Theoretical constraints on tidal triggering of slow earthquakes

Yishuo Zhou[1], Ankit Gupta[1,†], Hideo Aochi[1,2], Alexandre Schubnel[1], Satoshi Ide[3], Pierpaolo Dubernet[1], Harsha S. Bhat[1]

1. Laboratoire de Géologie, Ecole Normale Supérieure, CNRS-UMR 8538, PSL Research University, Paris, France
2. Bureau de Recherches Géologiques et Miniéres (BRGM), 45100 Orléans, France
3. Department of Earth and Planetary Science, The University of Tokyo, Tokyo, Japan

† Corresponding author: ankit.gupta@ens.fr

Keypoints: Tidal triggering; Small stress perturbations; Rate-and-state friction; Slow earthquakes; Frictional properties

CRediT

Conceptualization:	H. Aochi, A. Schubnel, H. S. Bhat
Methodology:	A. Gupta, Y. Zhou
Software:	A. Gupta, Y. Zhou, P. Dubernet
Investigation:	Y. Zhou, A. Gupta
Writing – original draft:	Y. Zhou
Writing – review & editing:	H. Aochi, A. Schubnel, H. S. Bhat, S. Ide, A. Gupta, Y. Zhou
Supervision:	H. Aochi, A. Schubnel, H. S. Bhat
Funding acquisition:	A. Schubnel, H. Aochi, H. S. Bhat

Abstract

Tidal stress is a globally acting perturbation driven primarily by the gravitational forcing of the Moon and the Sun. Understanding how tidal stresses can trigger seismic events is essential for constraining tectonic environments that are sensitive to small stress perturbations. Here, employing a spring–block with rate-and-state friction, we investigate tidal triggering on velocity-weakening stable sliding faults with stiffness slightly exceeding the critical stiffness. We first apply idealized step-like and boxcar normal stress perturbations to demonstrate a resonance-like amplification of slip rate when the perturbation period approaches the intrinsic frictional timescale of state evolution. Next, we perform nondimensional analyses and numerical simulations with harmonic tidal-like perturbations to identify the key parameters controlling tidal triggering and their admissible ranges. Triggered slip events are further characterized using physically interpretable quantities, including radiation efficiency and tidal phase. Our results show that even small stress perturbations can trigger periodic as well as complex slip events on stable sliding faults. The triggering behavior is primarily controlled by the normalized perturbation period and the normalized perturbation amplitude. An increase in the normalized period shifts event timing from the peak of tidal stress toward the peak of stress rate, whereas increasing the normalized amplitude promotes a transition from slow to fast events. The parameter space permitting triggered events suggests that the parameter which characterizes the instantaneous frictional strength of an interface, should not exceed tens to hundreds of kilopascals, and that the characteristic slip distance for frictional weakening is likely on the order of micrometers.

Plain Language Summary

Earth's crust experiences tiny but continuous stress changes caused by the gravitational pull of the Moon and Sun, known as tidal stresses. Although these stresses are very small, typically of the order of a few kilopascals and comparable to the pressure from a gentle hand press, they have been observed to trigger slow earthquakes on some faults. This raises an important question about the physical conditions under which faults become sensitive to such weak, periodic forces. Here, we show that even very weak tidal stresses can induce faults to slip through a process called resonance, much like pushing a swing at the right rhythm makes it move higher. We find that when the period of tidal stress perturbations matches the natural response timescale of a fault, the fault becomes significantly more sensitive to triggering. Using theoretical analysis and numerical simulations, we identify the specific combinations of fault properties and tidal characteristics that lead to slip events. Our work helps explain why some faults are unusually sensitive to tiny tidal forces and provide a way to infer fault properties from observations of tidally triggered slow earthquakes.

Keypoints

- Small persistent stress perturbations can trigger temporally complex slip events in otherwise stable sliding faults.
- Nondimensional framework presented can be generalized to various time-dependent perturbations, friction laws and continuum fault.
- Methodology to connect numerical events with observable quantities like: radiation efficiency and tidal phase.

1 Introduction

Slow earthquakes are a class of fault slip phenomena that release tectonic stress over timescales much longer than regular earthquakes, but shorter than long-term stable sliding. Over the past two and a half decades, slow earthquakes have been detected widely in many subduction zones around the Pacific Rim *(Schwartz & Rokosky 2007; Peng & Gomberg 2010).* Since they are predominantly observed both updip and downdip of megathrust seismogenic zones *(Obara & Kato 2016; Nishikawa et al. 2023),* slow earthquakes provide valuable insights into stress accumulation and release along plate interfaces and are therefore highly relevant for assessing the rupture potential and spatial extent of future megathrust earthquakes *(Obara 2025).*

Slow earthquakes can be broadly classified into five types, which are commonly grouped according to their detection methods as either seismic or geodetic. Seismically detected events, identified through ground shaking recorded by seismometers, include low-frequency earthquakes (LFEs), tectonic tremors (hereafter referred to as tremors), and very low-frequency earthquakes (VLFEs). Geodetically detected events, identified through crustal deformation measured by GNSS, strainmeters, or tiltmeters, include short-term and long-term slow slip events (SSEs). Among these phenomena, tremor is characterized by weak seismic signals lacking clear P- and S-wave arrivals *(Obara 2002),* with dominant frequencies in the 1–10 Hz range *(Shelly et al. 2007b; Obara 2020).* A key feature of tremor is its frequent spatial and temporal association with short-term SSEs, a coupled phenomenon now widely known as episodic tremor and slip (ETS) *(Rogers & Dragert 2003; Obara et al. 2004).* Because tremor is the most frequently detected signal, it is often used as a proxy for studying ETS *(Bartlow et al. 2011; Wech & Gomberg 2025).*

Another important feature of slow earthquakes, particularly tremors, is their high correlation with tidal stresses *(Ide & Tanaka 2014; Yabe et al. 2015; Ide et al. 2015; Hirose & Kobayashi 2025).* Tidal stress acting on the Earth arises from gravitational forcing by the Moon and the Sun, manifested through both solid Earth tides and ocean tidal loading, and produces well-characterized periodic stress perturbations with dominant periods of approximately 12 hours and amplitudes on the order of kilopascals ($\sim$ kPa). Early observations in southwest Japan and Cascadia showed that tremor occurrences often peak at intervals of about 12 and 24 hours, reflecting tidal periodicity *(Shelly et al. 2007a; Rubinstein et al. 2008; Nakata et al. 2008).* Motivated by these findings, subsequent studies have employed a variety of statistical approaches to quantify the relationship between tides and tremor occurrence, commonly by analyzing the distribution of tremors and LFEs with respect to tidal phase *(Thomas et al. 2012; Royer et al. 2015; Van Der Elst et al. 2016).*

A clear understanding of the physical mechanisms responsible for tidal modulation on tremor is therefore essential. Only with such an understanding can the observed sensitivity of tremor activity to tidal loading be meaningfully interpreted and used to constrain fault mechanical properties. Indeed, observational studies have shown that tremor exhibits a strong sensitivity to tidal loading and have argued, based on model-based interpretations, that this sensitivity implies very low effective normal stress, significantly lower than typical lithospheric megapascal-scale values, in regions hosting slow earthquakes *(Nakata et al. 2008; Thomas et al. 2009; Thomas et al. 2012; Yabe et al. 2015).* These inferences, however, critically depend on the assumed physical mechanisms linking tidal stress perturbations to tremor generation, motivating a range of modeling studies aimed at explaining the observed tidal correlations.

To address this model dependence, substantial efforts have been made in recent years to explore possible tidal triggering mechanisms using rate-and-state friction (RSF) models. In the RSF framework, fault behavior is primarily governed by the friction parameter $a - b$ *(Ruina 1983).* When $a - b < 0$, the fault exhibits velocity-weakening (VW) behavior, which favors stick-slip instabilities for stiffness below the critical value but stable sliding for stiffness above it. By contrast, when

$a-b>0$, velocity-strengthening (VS) behavior promotes stable sliding. A larger class of studies is based on the classical RSF formulation and focuses on VW faults or fractures that exhibit stick–slip behavior ($a-b<0$). These frameworks primarily explore how tidal stress modulates background seismicity. These models build on the seismicity rate theory of *Dieterich (1994),* which provides a time-dependent relationship between stress history and earthquake occurrence rate, and have been widely applied to explain periodic variations in seismicity at tidal and seasonal timescales *(Ader et al. 2014; Heimisson & Segall 2018; Heimisson & Avouac 2020; Dublanchet 2022; Udell-Lopez et al. 2026).* It is important to note that this class of models is primarily concerned with variations in event occurrence rates, rather than changes in event size or moment release. In a related but distinct line of work, *Mercuri & Rudnicki (2025)* examined the response of a single VW fault system to periodic perturbations from a dynamical perspective, explicitly resolving slip velocity and stick-slip cycles using a spring-block framework. This analysis focus on how periodic forcing amplifies or reshapes the slip dynamics of individual events, showing that the system response is controlled by the ratio T_p between the pore-pressure period and the intrinsic RSF timescale. For small T_p, pore pressure perturbations dominate and slip rate peaks align with pressure maxima, whereas for large T_p, intrinsic RSF instabilities dominate, leading to multiple slip events within a single perturbation cycle and a loss of phase locking.

Another class of models emphasizes the role of surrounding stable sliding in modulating seismic activity, based on the widely discussed view that LFEs occur on small VW patches embedded within predominantly VS fault zones. In this framework, tidal stresses may indirectly trigger LFEs by modulating the surrounding stable sliding, which in turn loads the patches and causes the seismicity rate to scale with the background stable sliding rate *(Ader et al. 2012). Ader et al. (2012)* investigated this mechanism using a spring-block model, focusing on the dynamical response of a stable sliding VS fault segment to periodic stress perturbations. Their results showed that periodic loading can strongly amplify slip velocity variations in near-velocity-neutral regions, and proposed that the tremor or LFE rate scales with the induced stable sliding velocity. This mechanism is supported by observations of deep LFEs on the San Andreas Fault (SAF) *(Beeler et al. 2013),* but it requires the presence of a sufficiently large, low-stiffness velocity-neutral region ($a-b\approx 0^+$, $k\ll k_c$), which may not exist in all tectonic environments.

Alternatively, *Perfettini et al. (2001)* studied perturbations acting directly on stable sliding of VW faults, without the need for modulation by surrounding creep, and identified a resonance phenomenon in which periodic loading can significantly amplify slip oscillations when the system is close to critical stiffness. This resonance behavior has been demonstrated experimentally by *Boettcher & Marone (2004) and Pignalberi et al. (2024)* and supported in observations *(Lowry 2006; Panda et al. 2018; Senapati et al. 2024; Sahoo et al. 2024).* Furthermore, some other physical processes have also been proposed to investigate tidal correlations. These include velocity-dependent transitions between VW and VS behavior *(Hawthorne & Rubin 2013),* dilatancy-induced strengthening *(Beeler et al. 2018; Sakamoto & Tanaka 2022; Zhao et al. 2025);* related studies have also examined slow slip and tremor associated with fluid-driven processes tremor in fault zones *(Yamashita & Suzuki 2011; Yamashita 2013).*

Building on the resonance mechanism identified by *Perfettini et al. (2001)* for VW faults undergoing stable sliding, our study moves beyond the identification of the mechanism itself and systematically investigates whether tidal stress perturbations can directly trigger slip events using a spring-block model. While Perfettini's work showed clearly the existence of the resonance phenomena in certain parameter sets, our study aims to explore more quantitatively, especially in the complex pattern of the triggered event in correlations to perturbation. We also clarify how resonance arises and becomes amplified during the triggering process. To this end, we first examine the response of a stable sliding VW fault to instantaneous normal stress perturbations, in order to characterize its fundamental transient behavior (Section 2). We then investigate the response to harmonic stress perturbations representative of tidal loading (Section 3). To capture the controlling mechanisms in a generalized form, a nondimensional framework is developed to identify the key control parameters that couple the properties of stress perturbations with the intrinsic frictional and dynamical properties of the fault (Section 3.2). Using spring–block simulations, we subsequently explore fault responses systematically across this parameter space, providing a unified physical interpretation of tidally triggered stable slip (Section 3.3). Then, we discuss the relationship between triggered events and tidal stress perturbations in the model, assess the robustness of these results to additional model parameters, and examine our model to tidal correlations observed in natural slow earthquakes in section 4. Finally, the main findings and their implications are summarized in section 5.

2 Fundamental response of stable sliding VW faults to instantaneous perturbations

A harmonic perturbation can be mathematically approximated by a boxcar perturbation that retains the same period and amplitude characteristics. A single boxcar perturbation, in turn, can be represented as two consecutive step-like perturbations of opposite sign, capturing the essential amplitude variations of the original harmonic perturbation. As a first step toward understanding the tidal response of a stable sliding VW fault, this section investigates the behavior under instantaneous normal stress changes, including both step and box loadings, to elucidate the fundamental mechanisms governing the system's response.

2.1 Governing equations of the spring-block model

We employ a spring–block model under stress perturbations (Figure 1), which allows for clear theoretical analysis. Under a constant normal stress σ_0, the fault, modeled as a point and elastically loaded by a spring, is subjected to normal stress perturbations $\sigma_{\mathrm{p}}(t)$ (positive in compression) and shear stress perturbations $\tau_{\mathrm{p}}(t)$ (positive in the direction of slip), resulting in a slip velocity V. We restrict our analysis to quasi-dynamic fault motion, as our focus is on the conditions under which tidal-like stress perturbations can trigger slip events, rather than on the detailed dynamics of rupture propagation.

The linear momentum balance of the spring-block system gives:

$$\tau_f = \sigma f = k(V_{\mathrm{ss}}\, t - \delta) - \eta V + \tau_{\mathrm{p}}(t) \tag{1}$$

$$\sigma = \sigma_0 + \sigma_{\mathrm{p}}(t) \tag{2}$$

where τ_f is the frictional resistance, σ is the total normal stress, f is the friction coefficient, k is the spring stiffness, V_{ss} is the slip velocity of the loading point, δ is the slip of the block and $V = d\delta/dt$ is the slip velocity of block. η represents the radiation damping coefficient, which approximates inertial effects and prevents the slip velocity from becoming unbounded during instabilities, and is given by $\eta = \mu/2c_s$, where μ is the shear modulus and c_s is the shear wave velocity *(Rice 1993)*.

We adopt the rate-and-state friction law (RSF) using the aging evolution law *(Dieterich 1979)*:

$$f = f_0 + a \log\left(\frac{V}{V_0}\right) + b \log\left(\frac{V_0 \theta}{d_c}\right) \tag{3}$$

$$\frac{d\theta}{dt} = 1 - \frac{V\theta}{d_c} \tag{4}$$

Here, f_0 is a reference friction coefficient when the fault is sliding at reference velocity V_0, as determined from laboratory rock friction experiments *(Marone 1998)*. θ is a state variable that characterizes the state of the sliding surfaces and has units of time. d_c is the characteristic slip distance for the evolution of θ. The parameters a, b are positive material constants. a represents the "direct effect", such that for fixed θ, the friction increases logarithmically with slip velocity, $\partial f/\partial \ln V > 0$. b characterizes the "evolution effect", describing the time-dependent weakening of friction through the evolution of the state variable. For $a - b = \partial f_{ss}/\partial \ln V_{\mathrm{ss}} > 0$ (VS regime; equivalently $a/b > 1$), friction increases with slip velocity, promoting stable sliding, whereas when $a-b < 0$ (VW regime; equivalently $0 < a/b < 1$), friction decreases with slip velocity and the fault may undergo unstable slip, if the spring stiffness is lower than a critical value ($k < k_c$); otherwise, stable sliding still occurs, characterized by smooth, quasi-static slip without sudden accelerations *(Ruina 1983; Rice & Ruina 1983)*.

In this study, we focus on a stable sliding VW fault, so we adopt $a/b = 0.9$ with $k/k_c = 1.1$. Although both normal stress $\sigma_{\mathrm{p}}(t)$ and shear stress $\tau_{\mathrm{p}}(t)$ perturbations are considered in the nondimensionalization (Sections 3.1), all subsequent simulations involving step, box and harmonic normal stress perturbations set $\tau_{\mathrm{p}}(t) = 0$ for simplicity. The details of the model parameters used in in Sections 2.2 and 2.3 are shown in Table 1.

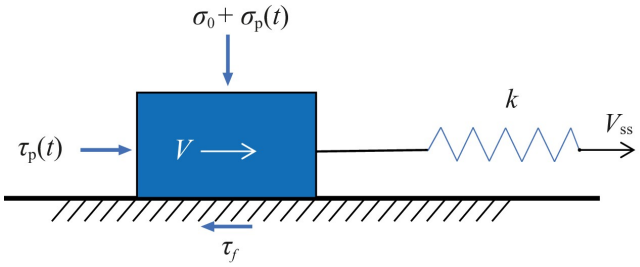

Figure 1: Spring–block model under stress perturbations. The block slides with velocity V under a constant normal stress σ_0, subject to an imposed normal stress perturbation $\sigma_p(t)$ and an applied shear stress perturbation $\tau_p(t)$. The elastic loading is provided by a spring of stiffness k, driven at a constant velocity V_{ss}. The resisting frictional shear stress is denoted by τ_f.

Table 1: Parameters used in numerical simulations of step and boxcar normal stress perturbation.

Parameter	Symbol	Value	Unit
Reference stable sliding friction coefficient	f_0	0.6	
Reference velocity	V_0	10^{-6}	m/s
RSF parameters	a/b	0.9	
Direct effect coefficient	a	0.0008	
Loading velocity	V_{ss}	10^{-9}	m/s
Characteristic slip distance	d_c	1×10^{-6}	m
Background (constant) normal stress	σ_0	1	MPa
Radiation damping coefficient	η	8×10^5	Pa · s/m
Spring stiffness	k	9.8×10^7	Pa/m

2.2 Response to a step change in normal stress

We examine the response of a stable sliding VW fault to instantaneous step changes in normal stress, prescribed as $\sigma_p(t) = \Delta\sigma H(t)$, where $H(t)$ is the Heaviside function. Both downward (tensile, $\Delta\sigma < 0$) and upward (compressive, $\Delta\sigma > 0$) step changes are considered. As the spring stiffness exceeds the critical stiffness, for both types of step changes the system exhibits a common response pattern: following the stress perturbation, the slip velocity displays a damped oscillatory evolution with progressively decaying amplitude toward stable sliding, as illustrated by the inset in Fig. 2a. Similar damped oscillatory behavior is also observed for a boxcar perturbation. Here, we focus in the following on the maximum slip velocity induced by each stress perturbation, which for step changes corresponds to the first peak in slip velocity following the perturbation.

2.2.1 Response to a tensile step change

Figure 2a shows the slip velocity response to a downward step change in normal stress ($\Delta\sigma < 0$). The response consists of two stages: an instantaneous increase in slip velocity at the moment of stress change (see Appendix A for a linear theoretical analysis of this instantaneous response), followed by a gradual acceleration toward a peak velocity. As the perturbation amplitude increases, the peak velocity becomes larger and is reached over a shorter time. This behavior is consistent with the results of *Paul et al. (2024),* who studied landslide dynamics using a block model without an elastic spring in the system. In contrast to that system, our model includes an elastic spring, which allows the slip velocity to recover after the peak, thereby preventing immediate runaway instabilities.

2.2.2 Response to an compressive step

Figure 2b shows the response to an upward step change in normal stress ($\Delta\sigma > 0$). In this case, the slip velocity decreases instantaneously at the time of the stress change, followed by an evolution phase during which the velocity reaches a local minimum before accelerating toward a peak. Larger compressive perturbations lead to higher peak velocities that occur

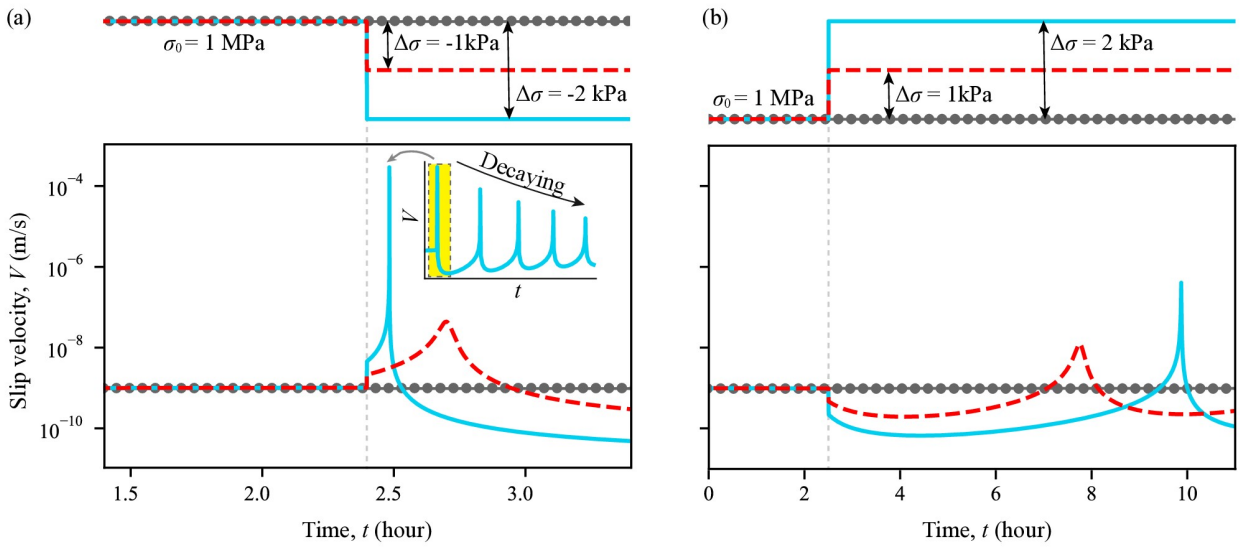

Figure 2: Responses of slip velocity to step changes in normal stress. (a) Downward step change and (b) Upward step change. Red dashed and blue solid curves correspond to $|\Delta\sigma| = 1$ kPa and 2 kPa, respectively. The dark gray line with circles indicates the reference case without stress perturbation. The inset in panel (a) illustrates the decaying oscillatory behavior of slip velocity following the transient step change. The other model parameters are listed in Table 1.

after longer times.

The contrasting (asymmetic) responses to tensile and compressive step changes reflect the opposite instantaneous effects of normal stress perturbations on frictional resistance. A sudden increase in normal stress strengthens the fault while the shear stress remains unchanged, causing the system to become more locked and delaying acceleration toward the peak slip velocity. In contrast, a tensile step reduces frictional resistance, facilitating slip and shortening the time required to reach the peak slip velocity.

2.3 Response to a boxcar change in normal stress

In this section, we examine the response of a stable sliding VW fault to finite-duration normal stress perturbations, prescribed as boxcar perturbations. A boxcar perturbation consists of two consecutive step changes of opposite polarity separated by a finite duration, $\sigma_{\rm p}(t) = \Delta\sigma\,[H(t-t_1) - H(t-t_2)]$, where $H(t)$ is the Heaviside function, $t_1 < t_2$, and $T_{\rm box} = t_2 - t_1$ denotes the duration of the perturbation. Depending on the sign of the initial step, the perturbation corresponds to either a box-up ($\Delta\sigma > 0$) or a box-down ($\Delta\sigma < 0$) loading. Here, we fix $|\Delta\sigma| = 1$ kPa. As in the step-change case (Section 2.2) and we characterize the fault response by the first peak slip velocity following the termination of the boxcar perturbation.

2.3.1 Response to a compressive change

We first consider the response to a box-up perturbation ($\Delta\sigma > 0$), in which an upward (compressive) step in normal stress is followed by a downward (tensile) step after a finite duration $T_{\rm box}$. Figure 3a shows the imposed normal stress histories for $T_{\rm box} = 15.6$ hours and 22.8 hours, together with the reference response to an upward step. The corresponding slip velocity responses are shown in the lower panel of Figure 3a.

As indicated by the dark gray curve with circles, an upward step change produces an initial peak in slip velocity, followed by a gradual decay toward stable sliding. This first peak defines the maximum slip velocity associated with the step response, $V_{\rm max}^{\rm step} \sim 10^{-8}$ m/s. For $T_{\rm box} = 15.6$ hours (red curve), the first peak slip velocity following the termination of the box-up perturbation reaching values of the order of 10^{-5} m/s, significantly larger than $V_{\rm max}^{\rm step}$. After this peak, the slip

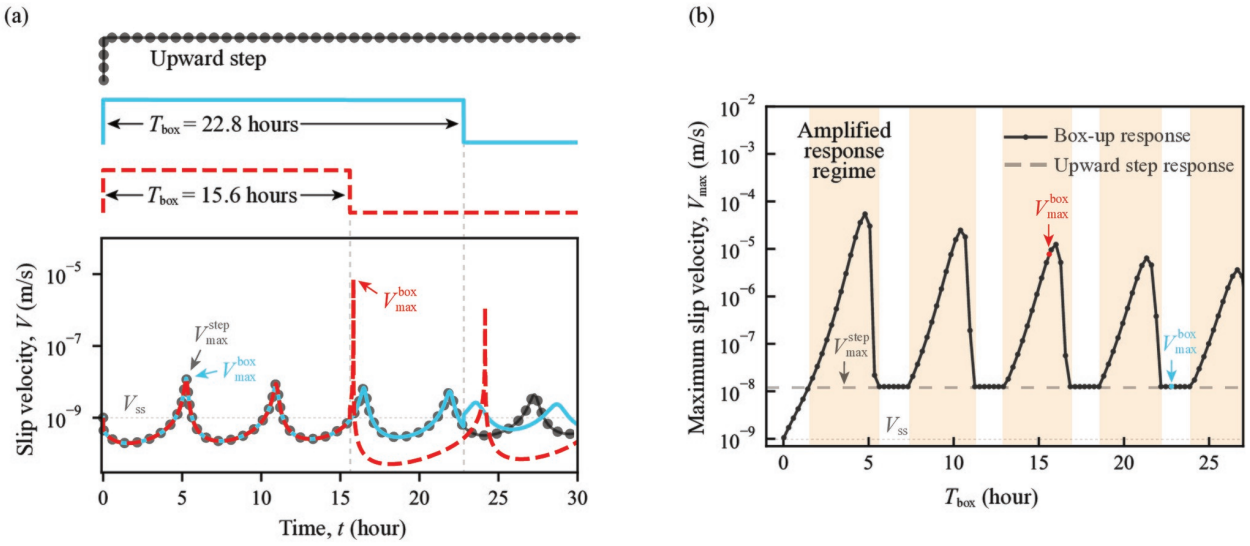

Figure 3: Responses of slip velocity to a box-up change in normal stress with $|\Delta\sigma| = 1.0$ kPa (the other model parameters are listed in Table 1). (a) Upper: imposed normal stress histories for $T_{box} = 22.8$ hours (blue) and 15.6 hours (red), compared with a single upward step (dark gray line with circles). Lower: corresponding slip velocity responses. (b) Maximum slip velocity V_{max} as a function of T_{box}. The shaded region highlights the range of T_{box} associated with amplified responses compared to the upward step change.

velocity again decays gradually, so that this post-termination peak defines the maximum slip velocity for this box-up case, V_{max}^{box}. In contrast, for $T_{box} = 22.8$ hours (blue curve), the first peak slip velocity following the termination of the box-up perturbation is lower than V_{max}^{step}, and the slip velocity subsequently decays. As a result, the maximum slip velocity in this case is given by the step-response peak, V_{max}^{step}.

To generalize these observations, Figure 3b shows the maximum slip velocity V_{max} as a function of T_{box}. For a fixed perturbation amplitude, an increase in slip velocity, relative to the step change response, occurs only over a limited range of perturbation periods, highlighted by the shaded region in the figure. Outside this range, the maximum velocity remains comparable to or smaller than V_{max}^{step}.

2.3.2 Response to a tensile change

We next consider the response to a box-down perturbation ($\Delta\sigma < 0$), in which a downward (tensile) step in normal stress is followed by an upward (compressive) step after a finite duration. The imposed normal stress histories for $T_{box} = 13.9$ hours and 22.8 hours are shown in the upper panel of Figure 4a, together with the reference response to a downward step. The corresponding slip velocity evolutions are shown in the lower panel.

As indicated by the dark gray curve with circles, a downward step produces a peak in slip velocity followed by a gradual decay toward stable sliding, defining the maximum slip velocity associated with the step response, V_{max}^{step}. For $T_{box} = 13.9$ hours (red curve), the post-termination peak exceeds the step response peak, whereas for $T_{box} = 22.8$ hours (blue curve), the post-termination peak remains lower than V_{max}^{step}. Figure 4b summarizes the maximum slip velocity V_{max} as a function of T_{box}. As in the box-up case, the enhancement of slip velocity relative to the step response occurs only for a limited range of perturbation periods, although the degree of enhancement and the corresponding T_{box} interval differ. Outside this range, the maximum slip velocity is controlled by the step response.

2.3.3 Summary: Resonance and velocity amplification

The analysis of step and finite-duration (boxcar) normal stress perturbations clarifies how transient stress changes are translated into slip acceleration on a stable sliding VW fault. Importantly, for a stable sliding VW fault, the slip response is strongly dependent on both the perturbation amplitude $\Delta\sigma$ and its duration T_{box}. Within some finite range of T_{box},

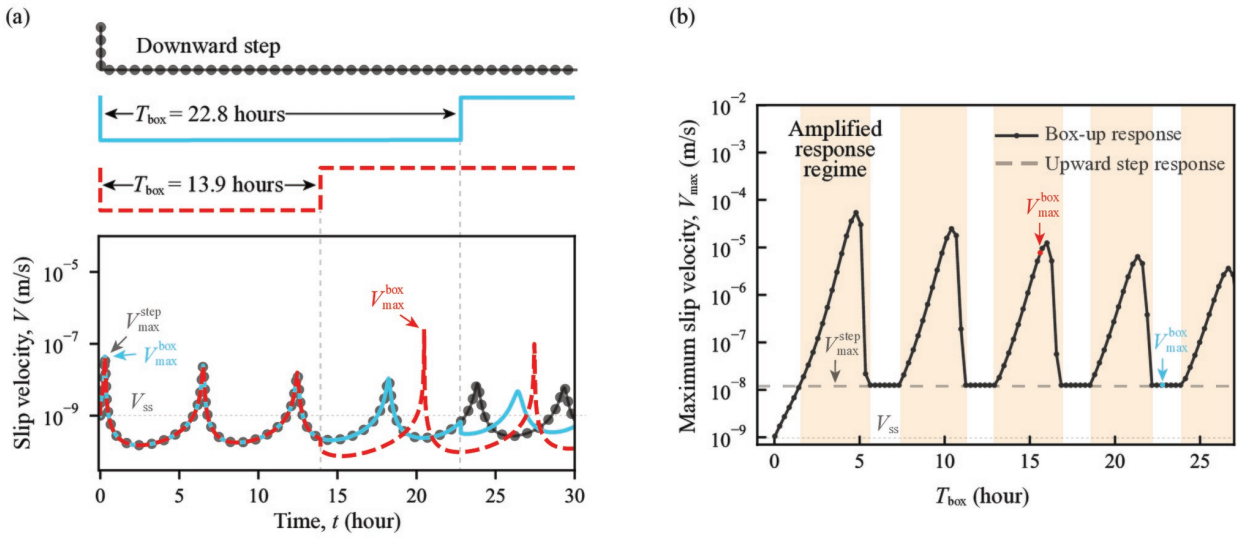

Figure 4: Responses of slip velocity to a box-down change in normal stress with $|\Delta\sigma| = 1.0$ kPa. (a) Upper: imposed normal stress histories for $T_{\rm box} = 22.8$ hours (blue) and 13.9 hours (red), compared with a single downward step (dark gray line with circles). Lower: corresponding slip velocity responses. (b) Maximum slip velocity $V_{\rm max}$ as a function of $T_{\rm box}$.

boxcar perturbations lead to a pronounced amplification of slip velocity relative to the corresponding step response, with peak velocities reaching up to several times larger than those of the corresponding response of the step change. Outside this range, the maximum slip velocity is largely controlled by the step-like response and no significant amplification occurs. This selective amplification indicates that when the duration of a finite-time stress perturbation approaches the intrinsic timescale of the fault system, the slip response can be strongly enhanced. Such behavior represents a clear manifestation of a resonance-like mechanism, in which the matching between the perturbation timescale and the system's internal timescale leads to amplified slip. This motivates the examination of harmonic, tidal-like stress perturbations in the following section.

3 Harmonic stress perturbation response of stable sliding VW faults

Building on the resonance-like behavior identified for step and boxcar perturbations, we now extend our analysis to tidal-like harmonic stress perturbations. Our goal is to determine the conditions under which such periodic forcing can generate observable slip acceleration on a stable sliding VW fault. It is noteworthy that, in stress perturbation problems, the system's response does not simply scale with the perturbation amplitude or period, but exhibits strong sensitivity to the fault's intrinsic properties. To capture this dependence in a general and physically transparent manner, we first perform a nondimensional analysis to identify the key control parameters that combine fault properties with perturbation characteristics. We then use numerical simulations to systematically explore the slip response across this parameter space, thereby delineating the regimes in which harmonic stress perturbations can effectively trigger significant slip events.

3.1 Scaling and nondimensional parameters

To identify the key factors controlling tidal triggering, we consider periodic, in-phase perturbations in both normal and shear stresses, expressed as $\sigma_{\rm p}(t) = \Delta\sigma \sin(2\pi t/T)$, $\tau_{\rm p}(t) = \Delta\tau \sin(2\pi t/T)$, where T is the tidal stress perturbation period. $\Delta\sigma$ is the amplitude of tidal normal stress (compression positive), and $\Delta\tau$ is the amplitude of tidal shear stress where an increase in shear stress in the direction of slip is assumed to be positive.

Building on the above model, we perform a nondimensional analysis to clarify the key factors controlling tidal triggering. Details of the derivation are given in Appendix B. The resulting formulation yields six nondimensional parameters (R_{ab}, κ, $\mathcal{N}$, ϵ, P_σ and P_T), each playing a critical role in governing fault dynamics.

The first nondimensional parameter is

$$R_{ab} = \frac{a}{b} \tag{5}$$

which controls the relative importance of frictional weakening and strengthening effects, where a, b are parameters in RSF framework. In steady state, the frictional response depends on the difference $(a-b)$, which governs whether friction increases or decreases with slip velocity. Steady-state VS occurs when $R_{ab} > 1$, velocity-neutral when $R_{ab} \to 1$, and VW when $0 < R_{ab} < 1$. Laboratory experiments indicate that R_{ab} typically exceeds 0.9 for VW surfaces *(Kilgore et al. 1993; Blanpied et al. 1998).* Moreover, in subduction zones, where constitutive properties vary primarily with temperature, the value of R_{ab} is expected to be close to 1 in the transition zone between locked and creeping regions, that is, between VW and VS regimes. This parameter R_{ab} is directly related to the quantity $R_b = (b-a)/b$ introduced by *Barbot (2019).* Physically, it is associated with the ratio between the stress drop, $\tau_0 - \tau_r \sim (b-a)\,\sigma_0$, and the frictional strength drop, $\tau_p - \tau_r \sim b\,\sigma_0$ *(Madariaga 1998; Erickson et al. 2008).* This quantity can be related to the commonly used S-ratio associated with the linear slip-weakening friction law, $\mathcal{S} = (\tau_p - \tau_0)/(\tau_0 - \tau_r) \sim a/(b-a) = R_{ab}/(1-R_{ab})$ *(Das 1976; Andrews 1976).*

The second nondimensional parameter is

$$\kappa = \frac{k}{k_c} \tag{6}$$

which controls the slip stability. *Ruina (1983)* showed that the critical spring stiffness is $k_c = (b-a)\,\sigma_0/d_c$. The system undergoes stable slip when $\kappa > 1$ and is unstable when $\kappa < 1$, showing stick-slip behavior .

The third nondimensional parameter is

$$\mathcal{N} = \frac{V_{\rm dyn}}{V_{\rm ss}} \tag{7}$$

which quantifies the relative importance of the radiation damping term in the model. The denominator is the stable sliding slip rate of the fault. The numerator $V_{\rm dyn} = a\sigma_0/\eta$ is a slip rate threshold beyond which the radiation damping term becomes effective, making the quasi-static assumption invalid *(Rubin & Ampuero 2005, Eq. A.8),* leading to the radiation of elastic seismic waves. This quantity can be interpreted as a metric that captures the relative importance of instantaneous frictional change to instantaneous elastic stress change.

The fourth nondimensional parameter is

$$\epsilon = \frac{\Delta\sigma}{\sigma_0} \tag{8}$$

which represents the ratio of tidal normal stress to the background (or constant) normal stress *(Perfettini et al. 2001).* Since the tidal normal stress is of the order of kPa, and the background (or constant) normal stress is usually of the order of MPa, this parameter is much smaller than 1, and it is not the controlling parameter for tide-induced triggering.

The fifth nondimensional parameter is

$$P_\sigma = \frac{|\Delta\tau - f_*^{\rm ss}\,\Delta\sigma\,|}{a\sigma_0} \tag{9}$$

which represents a normalized perturbation amplitude. The term f_{ss} denotes the steady-state friction coefficient at the background slip rate V_{ss}, is given by $f_{\rm ss}^* = f_0 + (a-b)\log\,(V_{\rm ss}/V_0)$. $|\Delta\tau - f_*^{\rm ss}\,\Delta\sigma\,|$ is the magnitude of tidal Coulomb stress change in the direction of slip in the context of the RSF. The tidal stress is a persistent loading and alternates periodically between positive and negative values. We are only interested in the long-term response of the fault and the sign of the tidal Coulomb stress change is inconsequential for understanding the dynamics of the system. The $a\sigma_0$

is the instantaneous frictional resistance offered by the fault. Thus, P_σ represents the ratio of Coulomb stress change and the instantaneous frictional strength change due to tidal perturbation. P_σ is closely related to the parameter $\mathcal{T} = (f_s\sigma_0 - \tau_0)/(f_s\Delta p_c)$ used in studies of induced seismicity, for which $P_\sigma \sim 1/\mathcal{T}$ *(Garagash & Germanovich 2012; Sáez et al. 2022).* The parameter $\mathcal{T}$ represents the ratio between the distance to failure $(f_s\sigma_0 - \tau_0)$ and the Coulomb stress change induced by fluid pressure $f_s\Delta p_c$. Under this interpretation, the quantity $a\sigma_0$ in RSF plays a role analogous to the distance to failure $(f_s\sigma_0 - \tau_0)$, where f_s is the static friction coefficient, τ_0 and σ_0 are the in-situ shear stress and background (or constant) normal stress, respectively. A smaller value of $a\sigma_0$, therefore implies that faults are more susceptible to small stress perturbations. Because $a\sigma_0$ is a material parameter and is independent of the in-situ shear stress state of the fault, faults operating above steady state, $\theta V/d_c > 1$, and characterized by very small $a\sigma_0$ may be regarded as critically stressed faults in RSF framework *(Garagash 2021).*

The last nondimensional parameter is

$$P_T = \frac{T}{t_*} = \frac{T\,V_{\rm ss}}{d_c} \tag{10}$$

which represents the perturbation period normalized by the characteristic state evolution timescale $t_* = d_c/V_{\rm ss}$. Here, T denotes the period of the imposed tidal-like sinusoidal stress perturbation, and t_* characterizes the timescale over which the state variable evolves in response to changes in slip rate *(Perfettini et al. 2001; Ader et al. 2012; Paul et al. 2024).* When $P_T \ll 1$, the perturbation period is short compared to the state evolution timescale, so the state variable remains effectively frozen over a forcing cycle. In this regime, the fault response is dominated by the direct velocity effect, characterized by the parameter a. In contrast, for $P_T \gg 1$, the perturbation varies slowly relative to state evolution, allowing the state variable to evolve during each cycle. As a result, the response approaches the steady-state frictional behavior controlled by $(b - a)$.

Analogously to $P_T = T/t_*$, the perturbation period can also be normalized by the elastic timescale as

$$P_{T2} = \frac{T}{t_a} = \frac{TkV_{\rm ss}}{a\sigma_0}, \tag{11}$$

which quantifies whether the external forcing varies slowly or rapidly compared to the elastic stress relaxation process. Here, an elastic–frictional timescale $t_a = a\sigma_0/(kV_{\rm ss})$ characterizes the rate at which stress perturbations are elastically transmitted and relaxed through the direct velocity effect under loading by a spring of stiffness k. This timescale governs the relaxation of the system following a stress perturbation and is responsible for the Omori-type decay predicted by the RSF framework *(Dieterich 1994).*

Among these parameters, the first three (R_{ab}, κ, $\mathcal{N}$) play key roles in controlling fault slip behavior and are already well understood in the absence of any external perturbations *(Barbot 2019; Wang 2024).* The remaining two parameters, P_σ and P_T, therefore emerge as the primary control parameters governing the fault response to stress perturbations. Although $\epsilon = \Delta\sigma/\sigma_0$ appears explicitly in the governing equations, we find that the system response is only weakly sensitive to this parameter over the range considered here. Accordingly, ϵ is fixed in the following analysis, allowing us to focus on the dominant control parameters P_σ and P_T.

Table 2: Model parameters used in numerical simulations of harmonic normal stress perturbations

nondimensional Parameter	**Symbol**	**Value**
Friction parameter	R_{ab}	0.9
Stiffness	κ	1.1
Radiation damping	$\mathcal{N}$	10^6
Stress perturbation	ϵ	10^{-3}
Perturbation amplitude	P_σ	$0.1 - 1$
Perturbation period	P_T	$1 - 100$

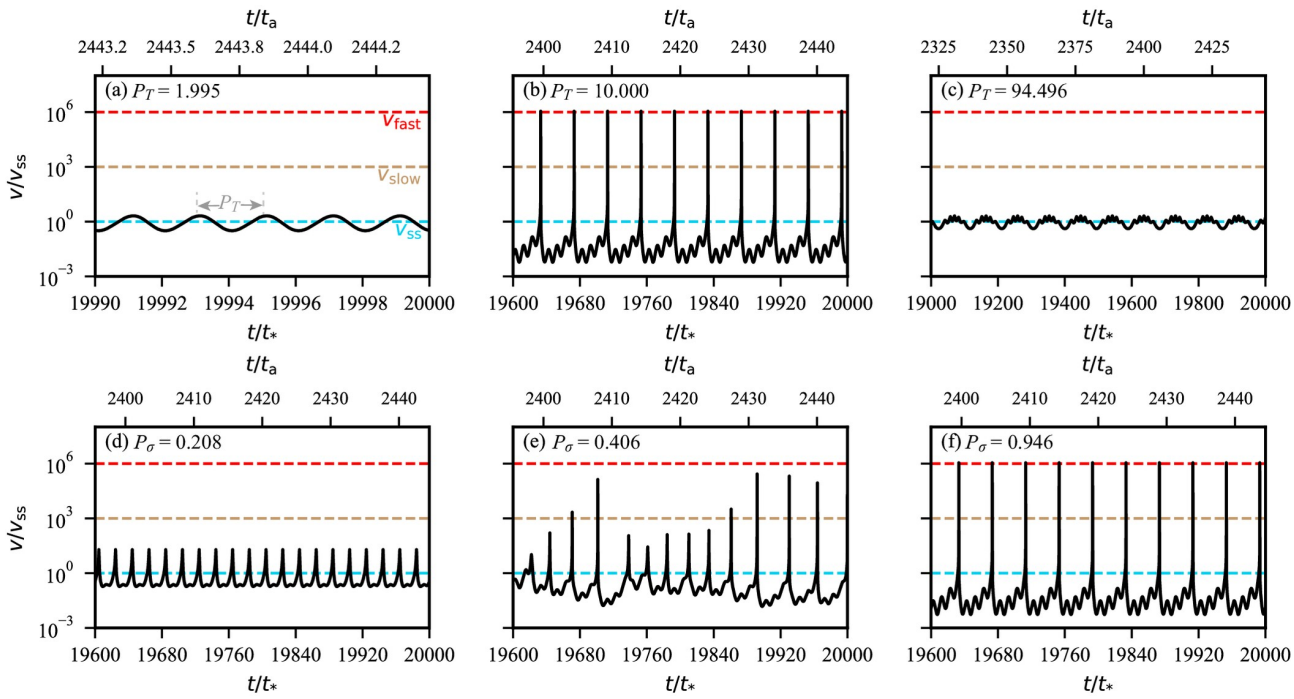

Figure 5: Normalized slip velocity $V/V_{\rm ss}$ as a function of time under periodic normal stress perturbations. Panels (a)-(c) show cases with fixed perturbation amplitude $P_\sigma = 0.892$ and increasing perturbation period $P_T = 1.995$, 10.000, and 94.496, respectively, illustrating a transition from creeping to episodic slip and back to quasi-creeping behavior. Panels (d)-(f) show cases with fixed perturbation period $P_T = 10.000$ and increasing perturbation amplitude $P_\sigma = 0.208$, 0.406, and 0.946, demonstrating progressively stronger slip responses. Dashed horizontal lines indicate velocity thresholds for stable sliding ($V/V_{\rm ss} = 1$), slow events (10^3), and fast events (10^6). Time is normalized by t_* (bottom axis) and by the elastic timescale t_a (top axis).

3.2 A phase diagram of slip behavior due to perturbations

We systematically explore the fault response to harmonic stress perturbations in the parameter space $P_\sigma \in [0.1, 1]$ and $P_T \in [1, 100]$. All other nondimensional parameters (R_{ab}, κ, $\mathcal{N}$, and ϵ) are held constant (Table 2). Because tidal stress amplitudes and periods are relatively well constrained (we adopt representative tidal values $\Delta\sigma = 1$ kPa and $T = 12$ hours here), varying P_σ and P_T effectively corresponds to exploring faults with different rheological characteristics. Slip behavior is analyzed within the time window $t/t_* = 10000 - 20000$ to ensure statistically steady conditions. Following previous studies, responses are classified based on the normalized slip velocity $V/V_{\rm ss}$: creeping for $V/V_{\rm ss} < 10^3$, slow slip events for $10^3 \leq V/V_{\rm ss} \leq 10^6$, and fast events for $V/V_{\rm ss} > 10^6$. Numerical implementation details, including the solver configuration and error control strategy, are provided in Appendix D.

Figure 5 illustrates representative normalized slip velocity responses under harmonic normal stress perturbations. Figures 5a–c show time series responses for different normalized perturbation periods P_T at a fixed amplitude $P_\sigma = 0.892$. As P_T increases, the fault response evolves non-monotonically, transitioning from creeping to slip events and eventually returning to a creeping state. This non-monotonic dependence reflects the competition between the timescale of the external forcing and the intrinsic timescale of the fault. For small P_T, the perturbation varies rapidly relative to the state evolution timescale, limiting the response to small, nearly instantaneous velocity oscillations that closely track the imposed stress. At intermediate P_T, where the forcing period becomes comparable to the state evolution timescale, the response is strongly amplified, producing slip events indicative of resonance-like behavior. For large P_T, the perturbation varies slowly enough for the state variable to fully adjust within each cycle, leading to quasi-static responses and suppression of dynamic slip instabilities.

Figure 5d-f presents slip velocity responses for a fixed perturbation period $P_T = 10$ and increasing perturbation amplitude P_σ. With increasing P_σ, the fault response evolves from weakly modulated creeping to slow slip events, and eventually to fast slip events, reflecting the progressively stronger influence of stress perturbations. In addition, intermediate amplitudes may produce complex or irregular slip patterns (as illustrated by case e), suggesting that the system can exhibit rich

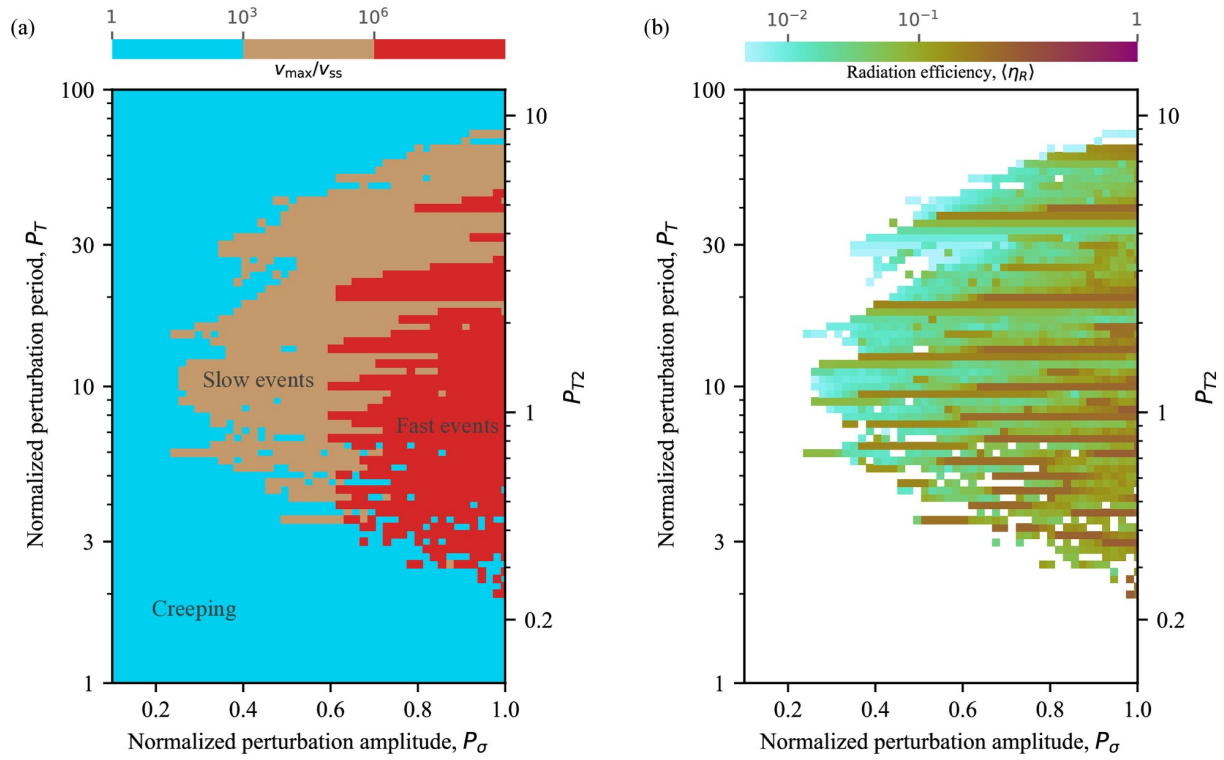

Figure 6: Response phase diagrams of a stable sliding VW fault in the (P_σ, P_T) parameter space under harmonic normal stress perturbations. (a) Phase diagram colored by the normalized maximum slip velocity $V_{\max}/V_{\rm ss}$. Light blue indicates creeping behavior, brown denotes slow slip events, and red corresponds to fast events.(b) The same parameter space colored by the average radiation efficiency $\langle \eta_R \rangle$, computed only for cases where slip events occur. An event is defined as a slip episode with $V_{\max}/V_{\rm ss} > 10^3$, and $\langle \eta_R \rangle$ represents the mean value averaged over all events in each simulation.

nonlinear dynamics even under purely harmonic forcing.

To synthesize the time series results described above, we construct a response phase diagram in the (P_σ, P_T) space (Figure 6a). The color scale represents the normalized maximum slip velocity, $V_{\max}/V_{\rm ss}$, which allows us to distinguish creeping behavior (light blue), slow slip events (brown), and fast slip events (red). The phase diagram reveals well-defined triggered events regimes, only within a confined region of parameter space, approximately $P_\sigma \gtrsim 0.2$ and $2 \lesssim P_T \lesssim 70$. Outside this window, the fault response remains creeping, with no detectable slip events. This result demonstrates that neither perturbation amplitude nor period alone is sufficient to trigger slip; instead, both must fall within specific ranges. By consolidating the transient responses into a single framework, the phase diagram provides a systematic and quantitative characterization of the conditions under which stress perturbations can trigger observable slip events on a stable sliding VW fault.

3.3 The radiation efficiency of triggered events

In the last section, we classified fast and slow events based on $V_{\max}/V_{\rm ss}$. Although the maximum slip velocity can indicate whether events occur under given tidal stress perturbations, it does not provide insight into the detailed slip dynamics, such as whether they are all fast or slow events. To address this limitation, we compute the average radiation efficiency, η_R, of all events (see Appendix C for details). This provides an alternative description of slip instabilities and is directly linked to the seismic energy radiated during an event *(Kostrov 1974).* Fast events exhibit high η_R, as a large fraction of the released potential energy is converted into seismic waves, whereas slow events have low η_R because almost all the available energy is dissipated on the fault. This distinction allows radiation efficiency also to provide insight into the relative proportion of fast versus slow events. Hereafter, we define events as slip events satisfying $V/V_{\rm ss} > 10^3$ within the time window $t/t_* = 10000$–20000, and compute the average radiation efficiency over all such events in each catalog. Because η_R spans several orders of magnitude, we use the geometric mean rather than the arithmetic mean: $\langle \eta_R \rangle = 10^{\langle \log \eta_R \rangle}$, where

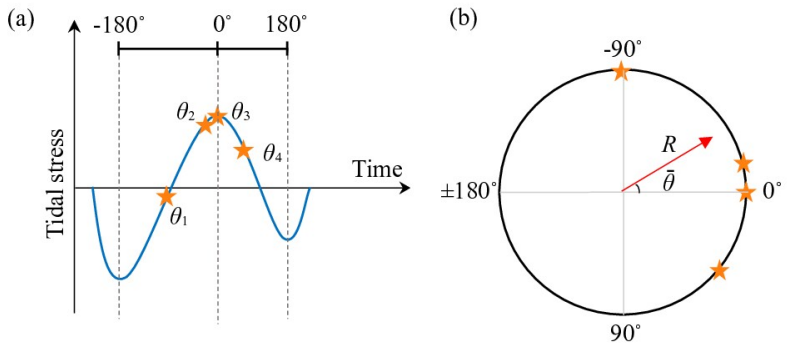

Figure 7: (a) Schematic showing the determination of the tidal phase θ. In the calculation of tidal phase, the stress peak closest to the event origin time is defined as 0°, while the adjacent troughs are set to –180° and +180°. The intervals from –180° to 0° and from 0° to +180° are evenly divided in time, allowing each moment to be assigned a corresponding phase. (b) Determination of the mean tidal phase $\bar{\theta}$ and the resultant vector length R.

$\langle \log \eta_R \rangle$ is the average of $\log \eta_R$ over all events in each catalog for a fixed duration.

Figure 6b presents the phase diagram of the average radiation efficiency within the event area of Figure 6a (here, the events as slip events satisfying $V/V_{\rm ss} > 10^3$, no distinguish slow and fast). We can find that larger P_σ systematically yields higher radiation efficiency, indicating that a greater fraction of the released energy is radiated as seismic waves. The values of P_T at which higher η_R (purple) occurs exhibit a comb-like distribution. This behavior can be understood in terms of the response to box stress perturbations. As discussed in Section 2.3, a box perturbation can be viewed as an upward stress step followed by a downward step. The timing of the downward step, which strongly influences the final response, is determined by the perturbation period P_T. For very small P_T, the system is still in the rising phase of the upward step response and has not yet reached its first peak when the downward step occurs, so the combined perturbation remains too weak to exceed the event threshold. For very large P_T, the peak response to the upward step has already relaxed back toward stable sliding before the downward step is applied, leaving the combined perturbation again ineffective. Only for intermediate values of P_T does the interaction between the upward and downward step responses produce sufficient amplification, giving rise to a series of discrete peaks in η_R (Figures 3b and 4b).

4 Discussion

4.1 The correlation between triggered events and tidal-like perturbations

In our simulations, tidal-like stress perturbations can trigger events on stable sliding VW fault due to resonance. A key subsequent question is whether the timing of these events correlates with the tidal stress, its rate of change, or shows no systematic relation. Addressing this issue is essential for assessing whether such resonance-driven triggering could be identified in natural observations.

Similar to the approaches used to study tidal correlations in natural (slow) earthquakes *(Thomas et al. 2012; Royer et al. 2015; Van Der Elst et al. 2016; Zhao et al. 2025),* we quantify the correlation using the tidal phase distribution. The tidal phase θ indicates the position within the tidal stress cycle at which an event occurs, distinguishing whether the event takes place near a tidal stress peak, a trough, or during the rising or falling stage. The definition of the tidal phase is illustrated in Figure 7a.

Because phase is a circular variable, the arithmetic mean is inappropriate (e.g., phase at $179°$ and $-179°$ are close, yet their arithmetic mean would misleadingly give $0°$). So to characterize the phase distribution, we employ two standard parameters from circular statistics: the mean tidal phase $\bar{\theta}$ and the resultant vector length R. As shown in Figure 7b, each

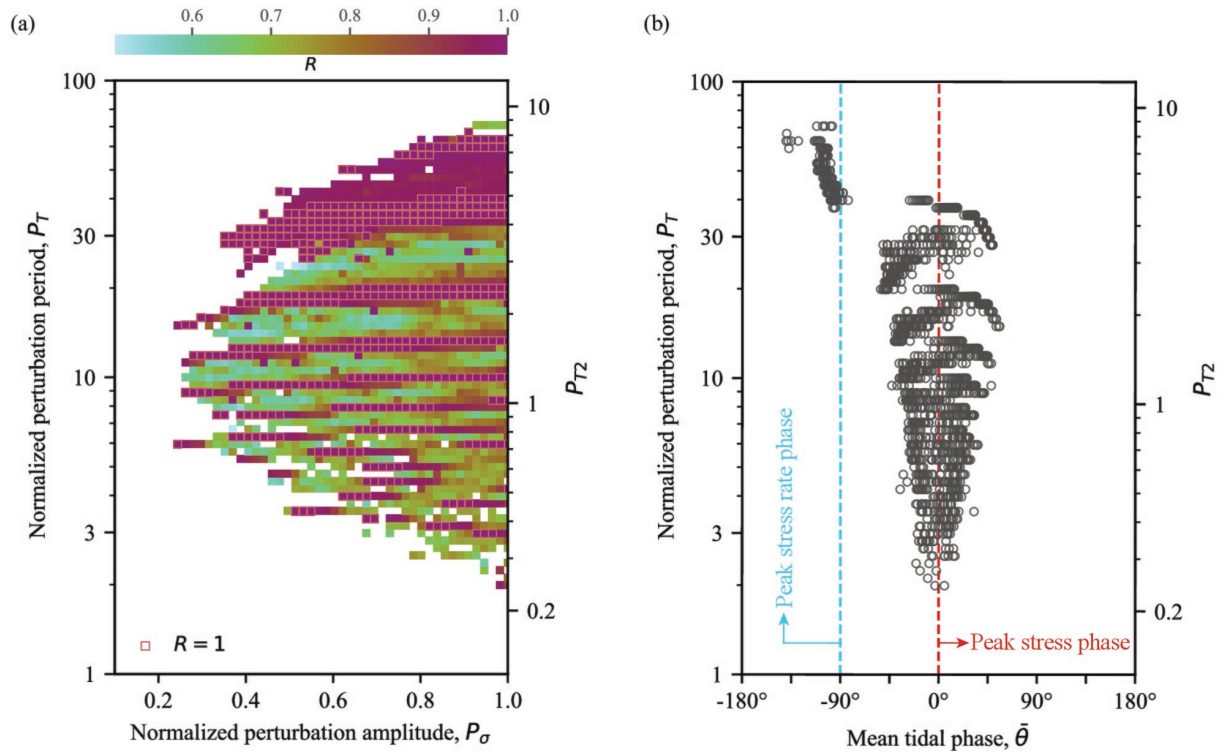

Figure 8: Correlation distribution of triggered events. (a) Phase concentration parameter R as a function of normalized perturbation amplitude P_σ and duration P_T, with color indicating the degree of phase clustering (larger R corresponds to stronger concentration around the mean phase). Red squares mark cases with $R = 1$. (b) Mean tidal phase $\bar{\theta}$ as a function of P_T. Each circle corresponds to the mean tidal phase calculated from a catalog of triggered events generated by a single simulation run at a given (P_σ, P_T) parameter combination. Vertical dashed lines indicate the peak stress phase 0° and the peak stress rate phase -90°.

phase θ is represented as a unit vector, and the components of the mean resultant vector are computed as:

$$\bar{x} = \frac{1}{N}\sum_{i=1}^{N}\cos\theta_i, \qquad \bar{y} = \frac{1}{N}\sum_{i=1}^{N}\sin\theta_i, \tag{12}$$

from which the mean tidal phase $\bar{\theta}$ is obtained as:

$$\bar{\theta} = \tan^{-1}\left(\frac{\bar{y}}{\bar{x}}\right) \tag{13}$$

which identifies a typical phase within the tidal cycle at which events preferentially occur. For example, $\bar{\theta} = 0^\circ$ indicates that events tend to occur near the peak tidal stress. $\bar{\theta} = -90^\circ$ corresponds to events occurring near the peak tidal stress rate.

The resultant vector length R quantifies the concentration of the phase distribution around $\bar{\theta}$:

$$R = \sqrt{\bar{x}^2 + \bar{y}^2}, \qquad 0 \le R \le 1 \tag{14}$$

A value of $R = 1$ indicates that all events occur at the same tidal phase. In contrast, smaller values of R indicate weaker phase clustering, with events distributed over a broader range of phases.

4.1.1 Evidence for resonant triggering

Figure 8a shows the tidal phase concentration R of triggered events. Overall, the events exhibit complex yet systematic tidal phase correlations across the explored parameter space. A particularly notable feature is the presence of cases with

$R = 1$ (red squares), indicating strong phase locking, where events repeatedly occur at the same tidal phase (though not necessarily in every tidal cycle). These phase-locked cases form a comb-like pattern along the P_T axis that largely coincides with the intervals of enhanced radiation efficiency η_R (Figure 6b), suggesting a close association between phase locking and amplified dynamic response. Notably, similar comb-like amplification is also identified in simulations with boxcar stress perturbation (e.g., Figure 3), where perturbations with specific perturbation periods produced pronounced slip velocity amplification. Together, these consistent patterns point to a common mechanism: when the perturbation period approaches a resonant timescale of the fault, slip amplification, increased radiation efficiency, and phase locking tend to emerge simultaneously. This consistency provides strong evidence that resonance governs tidal triggering in this regime.

4.1.2 Phase dependence of triggered events on P_T

When examining the mean tidal phase $\bar{\theta}$ of triggered events as a function of P_T, a clear systematic trend emerges (Figure 8b). For relatively large P_T (typically $P_T \gtrsim 40$), $\bar{\theta}$ clusters around $-90°$, indicating preferential occurrence near the phase of peak tidal stress rate. In contrast, for smaller P_T (approximately $P_T \lesssim 40$), $\bar{\theta}$ shifts toward around $0°$, suggesting a tendency for events to occur closer to the peak tidal stress. This dependence of phase preference on P_T provides a natural framework for interpreting tidal correlations observed in LFEs along the SAF *(Van Der Elst et al. 2016).* In that study, events cluster near $-90°$ when phases are evaluated using a longer-period (fortnightly) tidal stress envelope, whereas clustering near $0°$ is observed when phases are computed from semidiurnal tidal stresses. Our results further support one interpretation proposed by *Van Der Elst et al. (2016)* for the apparent $0°$ phase at semidiurnal periods. As illustrated by the time-series examples in Figure 5b, where small oscillations correspond to individual tidal cycles, in the small-P_T regime, instability may require multiple tidal cycles to develop, leading to an apparent alignment with the peak tidal stress rather than with the stress rate. A similar phase dependence was reported by *Bhatnagar et al. (2016)* for microseismicity at the East Pacific Rise, where seismicity preferentially occurred during phases of rapidly increasing fortnightly tidal stress. This behavior is consistent with the large-P_T regime identified in our simulations.

4.2 Influence of additional model parameters

All results presented above are obtained using the aging law for state evolution within the RSF framework. We also performed simulations using the slip law. As shown in B.2, the nondimensional parameters governing the triggering behavior remain unchanged when the slip law is adopted. Figures E1 and E2 (Appendix E) show that, compared to the aging law, the overall parameter range over which triggered events occur is nearly the same. The primary difference is that, in contrast to the aging law, the slip law tends to produce fast events, or events with higher radiation efficiency, at smaller normalized perturbation amplitude P_σ, that it is more easy to become instablity.

In addition, to account for variable normal stress, we additionally consider the formulation of *Linker & Dieterich (1992),* in which normal stress variations are coupled to the RSF evolution law. In this formulation, the modified state evolution law is $\dot{\theta}_L = \dot{\theta} - \alpha\theta\dot{\sigma}/b\sigma$, where α characterizes the sensitivity of the state variable to changes in normal stress. The detailed nondimensional derivation is presented in B.3. After nondimensionalization, the parameter α enters the definition of the normalized perturbation amplitude, $P_\sigma = (\Delta\tau - (f_*^{ss} - \alpha)\,\Delta\sigma)/(a\sigma_0)$. One extra nondimensional parameter, $\mathcal{L} = \alpha\epsilon/b$, appears in the evolution law, while all other nondimensional parameters remain unchanged. In the simulations presented above, we set $\alpha = 0$, such that $\mathcal{L} = 0 \ll 1$, and the inclusion of this effect does not qualitatively alter our results. For practical values of α such that $\mathcal{L} \sim \mathcal{O}(1)$, the influence of this parameter on the phase diagrams has yet to be quantified, but a systematic exploration of this regime is beyond the scope of the present study.

Moreover, a strong correlation with small-amplitude shear stress perturbations, but a comparatively weak correlation with large-amplitude normal stress variations, has been documented for LFEs along the SAF and for SSEs in Cascadia *(Thomas et al. 2009; Hawthorne & Rubin 2010).* As discussed by *Hawthorne & Rubin (2010) and Houston (2015),* one possible explanation for this weak response to normal stress variations is that fault slip occurs under undrained conditions, such that changes in normal stress are accompanied by compensating pore pressure variations. Let h_w [m] denote the hydraulic

width in the fault-normal direction and $c_d\,[\mathrm{m^2\,s^{-1}}]$ is the hydraulic diffusivity. The characteristic diffusion timescale in the fault-normal direction is then $T_d \sim h_w^2/c_d$. For the undrained approximation to be valid, this diffusion timescale must be much longer than both the tidal period, $T_d \gg T$, and the characteristic RSF timescale, $T_d \gg d_c/V_{\mathrm{ss}}$ *(Segall et al. 2010; Rudnicki & Mei 2025)*. If poroelastic effects are included (see B.4 for details), we find that the normalized stress perturbation amplitude can be written as $P_\sigma = |\Delta\tau - f_*^{ss}(1-B)\,\Delta\sigma|/(a\sigma_0')$, and that the normal stress perturbation parameter becomes $\epsilon = (1-B)\,\Delta\sigma/\sigma_0'$, where B is Skempton's coefficient and σ_0' denotes the reference effective normal stress. Consequently, the analysis presented above remains valid in the presence of poroelastic effects, provided that the nondimensional parameters P_σ and ϵ are redefined as above.

We further tested additional parameter combinations to examine the sensitivity of the triggering behavior, including variations in R_{ab}, κ, and $\mathcal{N}$. These variations do not alter the main qualitative conclusions reported here, and the detailed results are presented in Appendix F.

4.3 Relevance to tidal correlations in natural slow earthquakes

4.3.1 Constraints on frictional parameters

In this study, we have shown that tidal stresses can trigger events on stable sliding VW faults within a specific range of the nondimensional parameters P_T and P_σ ($P_\sigma \gtrsim 0.2$, and $2 \lesssim P_T \lesssim 70$). A key question is: within what range of structural and frictional parameters do these triggered events actually occur, and are these parameter regimes realistic in natural fault systems?

As discussed above, tidal stress in natural settings reflects the combined contributions of solid Earth tides and ocean tidal loading. It is well established that solid Earth tides typically induce stress changes of 0.1–5 kPa, while ocean tidal loading can generate stress perturbations reaching up to ~ 100 kPa in subduction zones *(Cochran et al. 2004; Zaccagnino et al. 2022)*. Taken together, these observations indicate that the effective tidal stress perturbation generally falls within the range 0.1–100 kPa. Here, we do not distinguish between the individual contributions from shear and normal stress perturbations, but instead consider their combined effect through the quantity $|\Delta\tau - f_*^{ss}\Delta\sigma|$. Combining this estimate with the normalized stress amplitude defined in our framework, $P_\sigma = |\Delta\tau - f_*^{ss}\,\Delta\sigma|/a\sigma_0$, we constrain $a\sigma_0$ to be in the range 0.5–500 kPa, where the lower (upper) bound corresponds to the lower (upper) end of the estimated tidal stress amplitude. This is consistent with the range inferred from tidal correlation analyses of real slow earthquakes. As shown in Table 3, observational studies involving tidal stress perturbations of order kilopascals (typically ∼0.1–a few kPa) consistently indicate low values of $a\sigma_0$, generally well below the MPa range. These estimates are consistent with the low $a\sigma_0$ values inferred from our modeling framework.

Table 3: A summary of $a\sigma_0$ values constrained from observation studies

References	Catalogs	Tidal stress (kPa)	Model	$a\sigma_0$ (kPa)
Nakata et al. (2008)	Nankai trough tremors	Coulomb stress ~ 1	*Dieterich (1994)*	1.3
Thomas et al. 2009; 2012	Parkfield tremors	shear stress ~ 0.1	*Dieterich (1994)*	$0.1-1$
Beeler et al. (2013)	SAF LFEs	shear stress ~ 0.4	*Ader et al. (2012)*	500
Yabe et al. (2015)	Nankai & Cascadia tremors	Coulomb stress $0-4$	*Ader et al. (2012)*	3
Royer et al. (2015)	northern Cascadia LFEs	shear stress ~ 2	*Beeler et al. (2013)*	7.6
Nakamura & Kakazu (2017)	Ryukyu Trench VLFEs	shear stress ~ 0.4	*Beeler et al. (2013)*	$1-2$

We now consider the nondimensional parameter $P_T = TV_{\mathrm{ss}}/d_c$, where T is the period of a tidal-like sinusoidal perturbation. Here, we consider the dominant tidal component with $T = 12$ hours. We assume that the event-generated patch is loaded by a quasi-steady background slip at rate V_{ss}, such that the characteristic timescale of the background slip is much longer than both the tidal period and the duration of the triggered slip events. This separation of timescales allows us to treat the background loading rate as effectively constant during tidal triggering. We consider two representative cases for

V_{ss}. The first case corresponds to the plate convergence rate *(DeMets et al. 2010)* or the long-term fault creep rate (the creeping section of the central SAF creeps at about 10^{-9} m/s *(Thomas et al. 2018).* For this case, d_c is estimated to lie between approximately 0.6 and 20 μm, consistent with values reported in laboratory rock-friction experiments *(Marone & Kilgore 1993; Marone 1998).* The second case corresponds to local slow slip velocities inferred from ETS, with V_{ss} in the range 10^{-8}–10^{-6} m/s *(Thomas et al. 2018; Rubin 2011).* For this case, the inferred values of d_c span approximately 6 μm to 2 cm. Although the upper bound of this estimate is relatively large, similar values have been proposed in the literature; for instance, *Maury et al. (2014)* estimated that a critical slip distance of 5 cm can reproduce the observed SSE in Mexico.

A lot of numerous studies consistently support a scale dependence of the characteristic slip distance d_c with event-generated patch size *(Gabriel et al. 2024). Rubin & Ampuero (2005)* demonstrated that fracture energy is approximately proportional to d_c within the RSF framework. *Ide & Aochi (2005)* proposed a hierarchical structure of patches in which the characteristic slip weakening distance, and hence the fracture energy *(Abercrombie & Rice 2005),* scales with patch size and controls earthquake nucleation and rupture propagation. Subsequently, *Hori & Miyazaki (2010), Nakata et al. (2023), Gerardi et al. (2024), and Almakari et al. (2025)* incorporated size-dependent d_c in RSF simulations of earthquake sequences. Laboratory experiments provide additional evidence for this scaling relationship: *Ohnaka (2003)* showed that the characteristic slip-weakening distance scales with fault heterogeneity or roughness, which itself increases with fault size.

The recent observation of *Zhao et al. (2025)* offers compelling support for this framework. They reported that ordinary earthquakes (OEs) at greater depths on the Central SAF are more sensitive to long-period hydrological loading, while shallow LFEs respond more strongly to short-period tidal loading. This dichotomy naturally aligns with size-dependent d_c: LFEs occur on small patches with correspondingly small d_c values, making them susceptible to shorter-period stress perturbations such as tides. In contrast, OEs rupture larger patches with larger d_c values and therefore respond more strongly to longer-period seasonal hydrological loading. This interpretation is consistent with our nondimensional framework, in which the sensitivity to periodic loading is controlled by the ratio $P_T \sim T/d_c$. Seasonal loading has a characteristic period of $T \sim 1$ year, approximately two orders of magnitude longer than the semidiurnal tidal period of $T \sim 12$ hours. For OEs to exhibit similar triggering sensitivity (i.e., similar values of P_T in our phase diagram), patches responding to seasonal loading must have d_c values approximately two orders of magnitude larger than those responding to tidal loading. This prediction agrees with the scaling of d_c with patches size if we accept that OEs occur on substantially larger patches than LFEs.

4.3.2 Implications, limitations, and observational consistency

In our simulations, the triggered catalogs are more appropriately interpreted as LFE-like events rather than tremors. LFEs are generally understood as repeating failures on a single patch, which is consistent with our modeling framework. Tremor, in contrast, is often interpreted as the superposition of many such LFEs occurring within a localized region *(Shelly et al. 2007b; Yabe & Ujiie 2025; Shelly et al. 2026).* It should be noted, however, that the present simulations consider a single patch in isolation and do not include interactions among multiple patches. As a result, collective effects that may be important for tremor generation are not explicitly captured in our model.

In this study, we focus on slip events that are distinct from creeping. Fast and slow events in our simulations are defined purely based on their slip velocities and are therefore model-based classifications, they do not necessarily correspond directly to fast or slow earthquakes observed in nature. It is worth noting, however, that the absence of such observations in nature does not necessarily imply that the phenomenon does not exist. As described by *Perfettini & Schmittbuhl (2001),* faults hosting fast earthquakes are not composed of a single homogeneous patch, and small variations in frictional and geometric properties can lead to substantial phase dispersion, making tidal correlations difficult to observe. Similarly, in our simulations, even for triggered events, the phase distribution can be highly scattered, which may explain why such correlations of fast earthquakes are rarely detected in natural observations.

Several observational studies have reported statistically significant tidal periodicities at subharmonic periods, most com-

monly near $\sim$ 6 h and $\sim$ 8 h, in catalogs of tremors in Taiwan and icequakes on the Ross Ice Shelf, even though these components are weak or nearly absent in the corresponding tidal stress records *(Chen et al. 2018; Yi-Chu et al. 2025; Udell-Lopez et al. 2026).* Our simulations demonstrate that enhanced radiation efficiency and phase locking emerge only at a discrete set of normalized perturbation periods, forming a comb-like pattern (Figures 6b and 8a). This indicates that, for a given frictional patch, triggered events can exhibit periodicity only under specific forcing conditions, rather than across a continuous range of periods. This suggests that, for a given frictional patch, triggered events can occur preferentially at specific forcing periods rather than across a continuous range, consistent with the isolated subharmonic periodicities reported in observations.

The phase relationship between events and tidal stresses in our simulations depends on P_T: for larger P_T, events are in phase with the tidal stress rate, while for smaller P_T, they are in phase with the tidal stress itself. Observationally, it is widely recognized that the tidal correlations of tremors during ETSs are weak in the early stages and become stronger in the later stages, both in the Nankai trough and Cascadia *(Houston 2015; Yabe et al. 2015).* Moreover, *Royer et al. (2015)* reported that on southern Vancouver Island, the phase relationship between LFEs and tidal stresses evolves from about -90° in the early stage to nearly 0° in the later stage. These evolutions can plausibly be attributed to a progressive decrease in the background slip velocity V_{ss}, for example from 10^{-6} to $10^{-8}\,\mathrm{m/s}$, corresponding to a decrease in P_T in our model. One discrepancy is that in our simulations the correlation with the tidal stress rate remains high even at large P_T, whereas in nature such a clear in-phase relation with the stress rate is not generally observed. This difference may arise because, in nature, the tidal stress rate signal is masked by the much stronger triggering influence of the underlying SSE itself.

A particularly noteworthy finding in our study is that periodic stress perturbations can even trigger complex slip events on faults that are otherwise stable sliding. This behavior arises from the intrinsic nonlinearity and history dependence of the RSF system. This behavior can be understood from the response to stress step changes. A stress step instantaneously displaces the system away from steady state, either to slip velocities above or below the steady state. Although the system tends to relax back toward steady state in both cases, upward and downward stress steps follow inherently different transient recovery paths, as discussed in Section 2.2.2.

Although this resonance-based framework is intentionally idealized and natural event catalogs are influenced by multiple interacting processes, it establishes the physical plausibility of resonance as a triggering mechanism and delineates the conditions under which it becomes effective. This mechanism may operate across a range of natural fault environments, from creeping segments such as the central creeping section of the SAF to regions characterized by ETS. Accordingly, the nondimensional parameter ranges identified here, together with local tidal characteristics and background slip rates, provide a practical framework for interpreting observed tidal correlations and for placing constraints on frictional parameters such as d_c and $a\sigma_0$. Therefore, while isolating resonance effects in natural observations remains challenging, revisiting this mechanism is nevertheless important given its potential role in shaping event triggering processes.

5 Conclusions

Building upon the seminal work of *Perfettini et al. (2001),* we here identify two key nondimensional parameters, normalized perturbation period P_T and stress amplitude P_σ, as controls of tidal triggering of instability on a stable velocity weakening fault. Within this framework, resonance emerges as a plausible mechanism linking tidal stress to slow earthquake activity identified ranges of these parameters. We further show that phase relationship depends systematically on P_T: for large P_T, triggered events occur in phase with the peak tidal stress rate, whereas for small P_T, they align with the peak tidal stress. Finally, the frictional parameters constrained by the nondimensional parameter ranges required for triggering are physically reasonable in natural fault conditions.

Acknowledgments

YZ, HA, HSB, SI, and AS gratefully acknowledge the support provided through the CNRS-University of Tokyo joint program SESAME. Part of the support was also provided by the European Research Council grant PERSISMO (grant

865411), including the computations conducted on the MADARIAGA HPC cluster at ENS, Paris. AS and HA acknowledge the support of ANR program PREMS (ANR-24-CE56-3575) as well as long standing fruitful discussions on the topic of tidal triggering with T. Hatano, F. Petrelis, K. Chanard and M. Colledge. AG acknowledges the support of LRC Yves Rocard postdoctoral funding from CEA, France. AG and HSB acknowledge the Indo-French SPARC grant for sponsoring NISER, Bhubaneswar visit which enabled fruitful discussions with Prof. Pathikrit Bhatacharya on modeling periodic perturbations on rate and state friction faults. AG and HSB also acknowledge discussions with Dr. Jorge Jara from GFZ Potsdam on the role of small perturbations in modulating seismicity. YZ and AG thank Dr. Navid Kheirdast from ISTeP, Paris for fruitful discussions on the energy budget of a event in quasi-dynamic simulations. YZ also thanks Caiyuan Fan, Bharath Shanmugasundaram and Suli Yao from ENS, Paris for helpful discussions. We also used LLM models like ChatGPT and Claude to debug/optimize our codes, and correct grammatical mistakes in the manuscript.

Open Research Section

The software, datasets generated and analyzed during this study, together with jupyter notebooks used in the analysis, are available via a Zenodo repository *(Zhou et al. 2026).*

Conflict of Interest

The authors declare no conflicts of interest relevant to this study.

References

Abercrombie, R. E. & J. R. Rice (2005). "Can observations of earthquake scaling constrain slip weakening?" In: *Geophysical Journal International* 162.2, pp. 406–424. DOI: 10.1111/j.1365-246X.2005.02579.x.

Ader, T. J., J.-P. Ampuero & J.-P. Avouac (2012). "The role of velocity-neutral creep on the modulation of tectonic tremor activity by periodic loading". In: *Geophysical Research Letters* 39.16, p. L16301. DOI: 10.1029/2012GL052326.

Ader, T. J., N. Lapusta, J.-P. Avouac & J.-P. Ampuero (2014). "Response of rate-and-state seismogenic faults to harmonic shear-stress perturbations". In: *Geophysical Journal International* 198.1, pp. 385–413. DOI: 10.1093/gji/ggu144.

Almakari, M, N Kheirdast, C Villafuerte, M. Thomas, P Dubernet, J Cheng, A Gupta, P Romanet, S Chaillat & H. Bhat (2025). "Spectrum of slip dynamics, scaling & statistical laws emerge from simplified model of fault and damage zone architecture". In: *arXiv preprint*. DOI: 10.48550/arXiv.2509.04909.

Andrews, D. J. (10, 1976). "Rupture Velocity of Plane Strain Shear Cracks". In: *Journal of Geophysical Research* 81.32, pp. 5679–5687. DOI: 10.1029/JB081i032p05679.

Barbot, S. (2019). "Slow-slip, slow earthquakes, period-two cycles, full and partial ruptures, and deterministic chaos in a single asperity fault". In: *Tectonophysics* 768, p. 228171. DOI: 10.1016/j.tecto.2019.228171.

Bartlow, N. M., S. Miyazaki, A. M. Bradley & P. Segall (2011). "Space-time correlation of slip and tremor during the 2009 Cascadia slow slip event". In: *Geophysical Research Letters* 38.18. DOI: 10.1029/2011GL048714.

Beeler, N. M., A. Thomas, R. Bürgmann & D. Shelly (2013). "Inferring fault rheology from low-frequency earthquakes on the San Andreas". In: *Journal of Geophysical Research: Solid Earth* 118.11, pp. 5976–5990. DOI: 10.1002/2013JB010118.

Beeler, N. M., A. Thomas, R. Bürgmann & D. Shelly (2018). "Constraints on friction, dilatancy, diffusivity, and effective stress from low-frequency earthquake rates on the deep San Andreas Fault". In: *Journal of Geophysical Research: Solid Earth* 123.1, pp. 583–605. DOI: 10.1002/2017JB015052.

Bhatnagar, T., M. Tolstoy & F. Waldhauser (2016). "Influence of fortnightly tides on earthquake triggering at the East Pacific Rise at 9 50' N". In: *Journal of Geophysical Research: Solid Earth* 121.3, pp. 1262–1279. DOI: 10.1002/2015JB012388.

Blanpied, M., C. Marone, D. Lockner, J. Byerlee & D. King (1998). "Quantitative measure of the variation in fault rheology due to fluid-rock interactions". In: *Journal of Geophysical Research: Solid Earth* 103.B5, pp. 9691–9712. DOI: 10.1029/98JB00162.

Boettcher, M. & C Marone (2004). "Effects of normal stress variation on the strength and stability of creeping faults". In: *Journal of Geophysical Research: Solid Earth* 109.B3. DOI: 10.1029/2003JB002824.

Cash, J. R. & A. H. Karp (1990). "A variable order Runge-Kutta method for initial value problems with rapidly varying right-hand sides". In: *ACM Transactions on Mathematical Software* 16.3, pp. 201–222. DOI: 10.1145/79505.79507.

Chen, K. H., H.-J. Tai, S. Ide, T. B. Byrne & C. W. Johnson (2018). "Tidal modulation and tectonic implications of tremors in Taiwan". In: *Journal of Geophysical Research: Solid Earth* 123.7, pp. 5945–5964. DOI: 10.1029/2018JB015663.

Cochran, E. S., J. E. Vidale & S. Tanaka (2004). "Earth tides can trigger shallow thrust fault earthquakes". In: *Science* 306.5699, pp. 1164–1166. DOI: 10.1126/science.1103961.

Das, S. (1976). "A Numerical Study Of Rupture Propagation And Earthquake Source Mechanism". PhD thesis. Massachusetts Institute of Technology.

DeMets, C., R. G. Gordon & D. F. Argus (2010). "Geologically current plate motions". In: *Geophysical journal international* 181.1, pp. 1–80. DOI: 10.1111/j.1365-246X.2009.04491.x.

Dieterich, J. (1994). "A constitutive law for rate of earthquake production and its application to earthquake clustering". In: *Journal of Geophysical Research: Solid Earth* 99.B2, pp. 2601–2618. DOI: 10.1029/93JB02581.

Dieterich, J. H. (1979). "Modeling of rock friction: 1. Experimental results and constitutive equations". In: *J. Geophys. Res.* 84.B5, pp. 2161–2168. DOI: 10.1029/JB084iB05p02161.

Dublanchet, P. (2022). "Seismicity modulation in a 3-D rate-and-state interacting fault population model". In: *Geophysical Journal International* 229.3, pp. 1804–1823. DOI: 10.1093/gji/ggac023.

Erickson, B., B. Birnir & D. Lavallée (2008). "A Model for Aperiodicity in Earthquakes". In: *Nonlinear Processes in Geophysics* 15.1, pp. 1–12. DOI: 10.5194/npg-15-1-2008.

Gabriel, A.-A., D. I. Garagash, K. H. Palgunadi & P. M. Mai (26, 2024). "Fault Size–Dependent Fracture Energy Explains Multiscale Seismicity and Cascading Earthquakes". In: *Science* 385.6707, eadj9587. DOI: 10.1126/science.adj9587.

Garagash, D. I. (2021). "Fracture Mechanics of Rate-and-State Faults and Fluid Injection Induced Slip". In: *Philosophical Transactions of the Royal Society A: Mathematical, Physical and Engineering Sciences* 379.2196, p. 20200129. DOI: 10.1098/rsta.2020.0129.

Garagash, D. I. & L. N. Germanovich (2012). "Nucleation and Arrest of Dynamic Slip on a Pressurized Fault: Nucleation on Pressurized Fault". In: *Journal of Geophysical Research: Solid Earth* 117.B10. DOI: 10.1029/2012JB009209.

Gerardi, G., P. Dublanchet, L. Jeannin, A. Kazantsev, L. Duboeuf, I. Ramadhan, H. Azis, N. Ganefianto & I. A. Nugroho (2024). "Geomechanical modelling of injection-induced seismicity: the case study of the Muara Laboh geothermal plant". In: *Geophysical Journal International* 237.2, pp. 818–837. DOI: 10.1093/gji/ggae084.

Hawthorne, J. C. & A. M. Rubin (2010). "Tidal Modulation of Slow Slip in Cascadia". In: *Journal of Geophysical Research: Solid Earth* 115.B9. DOI: 10.1029/2010JB007502.

Hawthorne, J. C. & A. M. Rubin (2013). "Tidal modulation and back-propagating fronts in slow slip events simulated with a velocity-weakening to velocity-strengthening friction law". In: *Journal of Geophysical Research: Solid Earth* 118.3, pp. 1216–1239. DOI: 10.1002/jgrb.50107.

Heimisson, E. R. & J.-P. Avouac (2020). "Analytical prediction of seismicity rate due to tides and other oscillating stresses". In: *Geophysical Research Letters* 47.23, e2020GL090827. DOI: 10.1029/2020GL090827.

Heimisson, E. R. & P. Segall (2018). "Constitutive law for earthquake production based on rate-and-state friction: Dieterich 1994 revisited". In: *Journal of Geophysical Research: Solid Earth* 123.5, pp. 4141–4156. DOI: 10.1029/2018JB015656.

Hirose, F. & A. Kobayashi (2025). "Tidal correlation of deep tectonic tremors increases during long-term slow slip events in the Bungo Channel, southwest Japan". In: *Earth, Planets and Space* 77.1, p. 18. DOI: 10.1186/s40623-025-02145-5.

Hori, T. & S. Miyazaki (2010). "Hierarchical asperity model for multiscale characteristic earthquakes: A numerical study for the off-Kamaishi earthquake sequence in the NE Japan subduction zone". In: *Geophysical Research Letters* 37.10. DOI: 10.1029/2010GL042669.

Houston, H. (2015). "Low friction and fault weakening revealed by rising sensitivity of tremor to tidal stress". In: *Nature Geoscience* 8.5, pp. 409–415. DOI: 10.1038/ngeo2419.

Ide, S. & H. Aochi (2005). "Earthquakes as multiscale dynamic ruptures with heterogeneous fracture surface energy". In: *Journal of Geophysical Research: Solid Earth* 110.B11. DOI: 10.1029/2004JB003591.

Ide, S. & Y. Tanaka (2014). "Controls on plate motion by oscillating tidal stress: Evidence from deep tremors in western Japan". In: *Geophysical Research Letters* 41.11, pp. 3842–3850. DOI: 10.1002/2014GL060035.

Ide, S., S. Yabe, H.-J. Tai & K. H. Chen (2015). "Thrust-type focal mechanisms of tectonic tremors in Taiwan: Evidence of subduction". In: *Geophysical Research Letters* 42.9, pp. 3248–3256. DOI: 10.1002/2015GL063794.

Kanamori, H. & T. H. Heaton (2000). "Microscopic and Macroscopic Physics of Earthquakes". In: *Geophysical Monograph Series*. Ed. by J. B. Rundle, D. L. Turcotte & W. Klein. Vol. 120. Washington, D. C.: American Geophysical Union, pp. 147–163. ISBN: 978-0-87590-978-3. DOI: 10.1029/GM120p0147.

Kheirdast, N, H. S. Bhat, M Almakari, A Gupta, C Villafuerte, M. Y. Thomas & P Dubernet (2025). "Energy budget of spectrum of slip dynamics emerging from simplified model of fault and damage zone architecture". In: *to be subm.* DOI: 10.48550/arXiv.2509.04909.

Kilgore, B. D., M. L. Blanpied & J. H. Dieterich (1993). "Velocity dependent friction of granite over a wide range of conditions". In: *Geophysical Research Letters* 20.10, pp. 903–906. DOI: 10.1029/93GL00368.

Kostrov, B. V. (1974). "Seismic moment and energy of earthquakes, and seismic flow of rock". In: *Izv. Acad. Sci. USSR Phys. Solid Earth* 1, pp. 23–44.

Linker, M. & J. H. Dieterich (1992). "Effects of variable normal stress on rock friction: Observations and constitutive equations". In: *Journal of Geophysical Research: Solid Earth* 97.B4, pp. 4923–4940. DOI: 10.1029/92JB00017.

Lowry, A. R. (2006). "Resonant slow fault slip in subduction zones forced by climatic load stress". In: *Nature* 442.7104, pp. 802–805. DOI: 10.1038/nature05055.

Madariaga, R (1998). *Complex Heterogeneous Faulting Models*.

Marone, C. (1998). "Laboratory-Derived Friction Laws and Their Application to Seismic Faulting". In: *Annual Review of Earth and Planetary Sciences* 26.1, pp. 643–696. DOI: 10.1146/annurev.earth.26.1.643.

Marone, C. & B. Kilgore (1993). "Scaling of the critical slip distance for seismic faulting with shear strain in fault zones". In: *Nature* 362.6421, pp. 618–621. DOI: 10.1038/362618a0.

Maury, J., H. Aochi & M. Radiguet (2014). "Fault constitutive relations inferred from the 2009-2010 slow slip event in Guerrero, Mexico". In: *Geophysical Research Letters* 41.14, pp. 4929–4936. DOI: 10.1002/2014GL060691.

Mercuri, M. & J. W. Rudnicki (2025). "Effects of Oscillating Pore Pressure of Fluid Injection on Fault Slip Described by Rate and State Friction". In: *Authorea Preprints*. DOI: 10.22541/essoar.176409493.34107389/v1.

Nakamura, M. & K. Kakazu (2017). "Tidal sensitivity of shallow very low frequency earthquakes in the Ryukyu Trench". In: *Journal of Geophysical Research: Solid Earth* 122.2, pp. 1221–1238. DOI: 10.1002/2016JB013348.

Nakata, R., N. Suda & H. Tsuruoka (2008). "Non-volcanic tremor resulting from the combined effect of Earth tides and slow slip events". In: *Nature Geoscience* 1.10, pp. 676–678. DOI: 10.1038/ngeo288.

Nakata, R., N. Uchida, T. Hori & R. Hino (2023). "Recurrence intervals for M¿ 7 Miyagi-ken-Oki earthquakes during an M˜ 9 earthquake cycle". In: *Progress in Earth and Planetary Science* 10.1, p. 34. DOI: 10.1186/s40645-023-00566-y.

Nishikawa, T., S. Ide & T. Nishimura (2023). "A review on slow earthquakes in the Japan Trench". In: *Progress in Earth and Planetary Science* 10.1, pp. 1–51. DOI: 10.1186/s40645-022-00528-w.

Obara, K. (2002). "Nonvolcanic deep tremor associated with subduction in southwest Japan". In: *Science* 296.5573, pp. 1679–1681. DOI: 10.1126/science.1070378.

Obara, K. (2020). "Characteristic activities of slow earthquakes in Japan". In: *Proceedings of the Japan Academy, Series B* 96.7, pp. 297–315. DOI: 10.2183/pjab.96.022.

Obara, K. (2025). "Where slow and large earthquakes meet". In: *Science* 388.6754, pp. 1369–1370. DOI: 10.1126/science.ady7173.

Obara, K., H. Hirose, F. Yamamizu & K. Kasahara (2004). "Episodic slow slip events accompanied by non-volcanic tremors in southwest Japan subduction zone". In: *Geophysical Research Letters* 31.23. DOI: 10.1029/2004GL020848.

Obara, K. & A. Kato (2016). "Connecting slow earthquakes to huge earthquakes". In: *Science* 353.6296, pp. 253–257. DOI: 10.1126/science.aaf1512.

Ohnaka, M. (2003). "A Constitutive Scaling Law and a Unified Comprehension for Frictional Slip Failure, Shear Fracture of Intact Rock, and Earthquake Rupture". In: *Journal of Geophysical Research: Solid Earth* 108.B2, 2000JB000123. DOI: 10.1029/2000JB000123.

Panda, D., B. Kundu, V. K. Gahalaut, R. Bürgmann, B. Jha, R. Asaithambi, R. K. Yadav, N. K. Vissa & A. K. Bansal (2018). "Seasonal modulation of deep slow-slip and earthquakes on the Main Himalayan Thrust". In: *Nature communications* 9.1, p. 4140. DOI: 10.1038/s41467-018-06371-2.

Paul, K., P. Bhattacharya & S. Misra (2024). "Frictional control on accelerating creep during the slow-to-fast transition of rainfall-induced catastrophic landslides". In: *Journal of Geophysical Research: Earth Surface* 129.1, e2023JF007213. DOI: 10.1029/2023JF007213.

Peng, Z. & J. Gomberg (2010). "An integrated perspective of the continuum between earthquakes and slow-slip phenomena". In: *Nature geoscience* 3.9, pp. 599–607. DOI: 10.1038/ngeo940.

Perfettini, H. & J. Schmittbuhl (2001). "Periodic loading on a creeping fault: Implications for tides". In: *Geophysical Research Letters* 28.3, pp. 435–438. DOI: 10.1029/2000GL011686.

Perfettini, H., J. Schmittbuhl, J. R. Rice & M. Cocco (2001). "Frictional response induced by time-dependent fluctuations of the normal loading". In: *Journal of Geophysical Research: Solid Earth* 106.B7, pp. 13455–13472. DOI: 10.1029/2000JB900366.

Pignalberi, F., C. Giorgetti, C. Noël, C. Marone, C. Collettini & M. M. Scuderi (2024). "The effect of normal stress oscillations on fault slip behavior near the stability transition from stable to unstable motion". In: *Journal of Geophysical Research: Solid Earth* 129.2, e2023JB027470. DOI: 10.1029/2023JB027470.

Rice, J. R., N. Lapusta & K. Ranjith (2001). "Rate and state dependent friction and the stability of sliding between elastically deformable solids". In: *J. Mech. Phys. Solids* 49.9, pp. 1865–1898. DOI: 10.1016/S0022-5096(01)00042-4.

Rice, J. R. (1993). "Spatio-temporal complexity of slip on a fault". In: *Journal of Geophysical Research: Solid Earth* 98.B6, pp. 9885–9907. DOI: 10.1029/93JB00191.

Rice, J. R. & A. L. Ruina (1983). "Stability of steady frictional slipping". In: *J. Appl. Mech.* 50, pp. 343–349. DOI: 10.1115/1.3167042.

Rogers, G. & H. Dragert (2003). "Episodic tremor and slip on the Cascadia subduction zone: The chatter of silent slip". In: *Science* 300.5627, pp. 1942–1943. DOI: 10.1126/science.1084783.

Royer, A., A. Thomas & M. Bostock (2015). "Tidal modulation and triggering of low-frequency earthquakes in northern Cascadia". In: *Journal of Geophysical Research: Solid Earth* 120.1, pp. 384–405. DOI: 10.1002/2014JB011430.

Rubin, A. M. (2011). "Designer friction laws for bimodal slow slip propagation speeds". In: *Geochemistry, Geophysics, Geosystems* 12.4. DOI: 10.1029/2010GC003386.

Rubin, A. M. & J.-P. Ampuero (2005). "Earthquake nucleation on (aging) rate and state faults". In: *Journal of Geophysical Research: Solid Earth* 110.B11. DOI: 10.1029/2005JB003686.

Rubinstein, J. L., M. La Rocca, J. E. Vidale, K. C. Creager & A. G. Wech (2008). "Tidal modulation of nonvolcanic tremor". In: *Science* 319.5860, pp. 186–189. DOI: 10.1126/science.1150558.

Rudnicki, J. W. & C. Mei (2025). "Homogeneous and Membrane Pore Fluid Diffusion in Spring Block Simulations of Fault Slip With Rate and State Friction". In: *Journal of Geophysical Research: Solid Earth* 130.12, e2025JB032174. DOI: 10.1029/2025JB032174.

Ruina, A. (1983). "Slip instability and state variable friction laws". In: *J. Geophys. Res.* 88.10, pp. 359–370. DOI: 10.1029/JB088iB12p10359.

Sáez, A., B. Lecampion, P. Bhattacharya & R. C. Viesca (2022). "Three-Dimensional Fluid-Driven Stable Frictional Ruptures". In: *Journal of the Mechanics and Physics of Solids* 160, p. 104754. DOI: 10.1016/j.jmps.2021.104754.

Sahoo, S., B. Senapati, D. Panda, S. Jin & B. Kundu (2024). "Tidal triggering of seismic swarm associated with hydrothermal circulation at Blanco ridge transform fault zone, Northeast Pacific". In: *Physics of the Earth and Planetary Interiors* 356, p. 107259. DOI: 10.1016/j.pepi.2024.107259.

Sakamoto, R. & Y. Tanaka (2022). "Frictional and hydraulic properties of plate interfaces constrained by a tidal response model considering dilatancy/compaction". In: *Journal of Geophysical Research: Solid Earth* 127.8, e2022JB024112. DOI: 10.1029/2022JB024112.

Schwartz, S. Y. & J. M. Rokosky (2007). "Slow slip events and seismic tremor at circum-Pacific subduction zones". In: *Reviews of Geophysics* 45.3. DOI: 10.1029/2006RG000208.

Segall, P. (2010). *Earthquake and Volcano Deformation*. Princeton, N.J: Princeton University Press. 432 pp. ISBN: 978-0-691-13302-7.

Segall, P., A. M. Rubin, A. M. Bradley & J. R. Rice (2010). "Dilatant Strengthening as a Mechanism for Slow Slip Events". In: *Journal of Geophysical Research: Solid Earth* 115.B12. DOI: 10.1029/2010JB007449.

Senapati, B., B. Kundu, B. Jha & S. Jin (2024). "Gravity-induced seismicity modulation on planetary bodies and their natural satellites". In: *Scientific Reports* 14.1, p. 2311. DOI: 10.1038/s41598-024-52809-7.

Senatorski, P. (2014). "Radiated Energy Estimations from Finite-fault Earthquake Slip Models". In: *Geophysical Research Letters* 41.10, pp. 3431–3437. DOI: 10.1002/2014GL060013.

Shelly, D. R., G. C. Beroza & S. Ide (2007a). "Complex evolution of transient slip derived from precise tremor locations in western Shikoku, Japan". In: *Geochemistry, Geophysics, Geosystems* 8.10. DOI: 10.1029/2007GC001640.

Shelly, D. R., G. C. Beroza & S. Ide (2007b). "Non-volcanic tremor and low-frequency earthquake swarms". In: *Nature* 446.7133, pp. 305–307. DOI: 10.1038/nature05666.

Shelly, D. R., A. M. Thomas, K. Z. Materna & R. J. Skoumal (2026). "Low-frequency earthquakes track the motion of a captured slab fragment". In: *Science* 391.6782, pp. 294–299. ISSN: 1095-9203. DOI: 10.1126/science.aeb2407.

Thomas, A., N. M. Beeler, Q. Bletery, R. Burgmann & D. R. Shelly (2018). "Using low-frequency earthquake families on the San Andreas Fault as deep creepmeters". In: *Journal of Geophysical Research: Solid Earth* 123.1, pp. 457–475. DOI: 10.1002/2017JB014404.

Thomas, A., R Bürgmann, D. R. Shelly, N. M. Beeler & M. Rudolph (2012). "Tidal triggering of low frequency earthquakes near Parkfield, California: Implications for fault mechanics within the brittle-ductile transition". In: *Journal of Geophysical Research: Solid Earth* 117.B5. DOI: 10.1029/2011JB009036.

Thomas, A. M., R. M. Nadeau & R. Bürgmann (2009). "Tremor-tide correlations and near-lithostatic pore pressure on the deep San Andreas fault". In: *Nature* 462.7276, pp. 1048–1051. DOI: 10.1038/nature08654.

Udell-Lopez, K., M.-H. Huang & V. Lekić (2026). "Using rate-and-state friction constitutive laws to predict seismicity rates for ice rifts on the Ross Ice Shelf in Antarctica". In: *Earth and Planetary Science Letters* 675, p. 119790. ISSN: 0012-821X. DOI: 10.1016/j.epsl.2025.119790.

Van Der Elst, N. J., A. A. Delorey, D. R. Shelly & P. A. Johnson (2016). "Fortnightly modulation of San Andreas tremor and low-frequency earthquakes". In: *Proceedings of the National Academy of Sciences* 113.31, pp. 8601–8605. DOI: 10.1073/pnas.1524316113.

Venkataraman, A. (2002). "Investigating the Mechanics of Earthquakes Using Macroscopic Seismic Parameters". PhD thesis. California Institute of Technology.

Wang, S. (2024). "Toward Quantitative Characterization of Simulated Earthquake-Cycle Complexities". In: *Scientific Reports* 14.1, p. 16811. DOI: 10.1038/s41598-024-67685-4.

Wech, A. G. & J. Gomberg (2025). "Rupture continuity through intermittent pauses in Cascadia slow slip events". In: *Journal of Geophysical Research: Solid Earth* 130.8, e2025JB031501. DOI: 10.1029/2025JB031501.

Yabe, S. & K. Ujiie (2025). "Tectonic Tremor Explained by Successive Ruptures of Clustered Quartz-Filled Shear Veins". In: *Geophysical Research Letters* 52.14. DOI: 10.1029/2025gl115447.

Yabe, S., Y. Tanaka, H. Houston & S. Ide (2015). "Tidal sensitivity of tectonic tremors in Nankai and Cascadia subduction zones". In: *Journal of Geophysical Research: Solid Earth* 120.11, pp. 7587–7605. DOI: 10.1002/2015JB012250.

Yamashita, T. (2013). "Generation of slow slip coupled with tremor due to fluid flow along a fault". In: *Geophysical Journal International* 193.1, pp. 375–393. DOI: 10.1093/gji/ggs117.

Yamashita, T. & T. Suzuki (2011). "Dynamic modeling of slow slip coupled with tremor". In: *Journal of Geophysical Research: Solid Earth* 116.B5. DOI: 10.1029/2010JB008136.

Yi-Chu, H., K. H. Chen, S. Ide & P.-Y. P. Lin (2025). "Characteristics and generation mechanisms of tremors across a mountain belt". In: *Tectonophysics*, p. 231036. DOI: 10.1016/j.tecto.2025.231036.

Zaccagnino, D., L. Telesca & C. Doglioni (2022). "Correlation between seismic activity and tidal stress perturbations highlights growing instability within the brittle crust". In: *Scientific Reports* 12.1, p. 7109. DOI: 10.1038/s41598-022-11328-z.

Zhao, Z., L. Xue, R. Bürgmann, E. R. Heimisson, W. Lu & H. Yue (2025). "Tidal and hydrological seismicity modulations reveal pore fluid diffusion during earthquake nucleation". In: *Science Advances* 11.49. DOI: 10.1126/sciadv.ady6350.

Zhou, Y., A. Gupta, H. Aochi, A. Schubnel, S. Ide, P. Dubernet & H. Bhat (2026). *Data and code for: Theoretical constraints on tidal triggering of slow earthquakes*. Version v1. DOI: 10.5281/zenodo.18454815.

Appendix A Response of a stable sliding RSF fault to instantaneous shear and normal stress perturbations

The instantaneous increase in system velocity (i.e., the amplitude of the instantaneous velocity perturbation during the first phase) originates from the requirement to satisfy quasi-static equilibrium between the background shear traction and the frictional strength at the moment of a stress step. Here, we consider an instantaneous change in shear stress from τ_0 to $\tau_0 + \Delta\tau_{\text{step}}$, accompanied by a normal stress change from σ_0 to $\sigma_0 + \Delta\sigma_{\text{step}}$, following *Paul et al. (2024).*

Under RSF with the Linker–Dieterich evolution law*(Linker & Dieterich 1992),* both the friction coefficient and the state variable undergo instantaneous changes in response to a shear and normal stress step. The friction coefficient responds through the direct effect associated with a sudden change in sliding velocity, while the state variable experiences an instantaneous jump induced by the normal stress perturbation. Immediately before the stress perturbation, the fault is in quasi-static equilibrium and sliding at steady state ($\theta_{\text{ss}} V_{\text{ss}}/d_c = 1$), such that

$$\tau_0 = f_{\text{ss}}\, \sigma_0, \tag{A1}$$

where

$$f_{\text{ss}} = f_0 + (a-b)\log\left(\frac{V_{\text{ss}}}{V_0}\right), \tag{A2}$$

and V_{ss} is the steady-state sliding velocity prior to the perturbation and θ_{ss} is corresponding state variable.

Immediately after the stress step, equilibrium requires

$$\tau_0 + \Delta\tau_{\text{step}} = f_2\left(\sigma_0 + \Delta\sigma_{\text{step}}\right), \tag{A3}$$

where $f_2 = f_0 + (a-b)\log\left(\frac{V_2}{V_0}\right) + b\log\left(\frac{\theta_2 V_2}{d_c}\right)$. Subtracting the pre-step equilibrium condition from the post-step condition yields

$$\Delta\tau_{\text{step}} = (f_2 - f_{\text{ss}})(\sigma_0 + \Delta\sigma_{\text{step}}) + f_{\text{ss}}\Delta\sigma_{\text{step}} \tag{A4}$$

During the instantaneous normal stress step, the slip is zero. Consequently, the state variable does not evolve through slip but changes according to the Linker-Dieterich normal-stress effect, which can be obtained by solving $\int_{\theta_{\text{ss}}}^{\theta_2} \frac{d\theta}{\theta} = -\frac{\alpha}{b}\int_{\sigma_0}^{\sigma_0+\Delta\sigma_{\text{step}}} \frac{d\sigma}{\sigma}$, across the normal step,

$$\theta_2 = \theta_{\text{ss}}\left(\frac{\sigma_0 + \Delta\sigma_{\text{step}}}{\sigma_0}\right)^{-\frac{\alpha}{b}}, \tag{A5}$$

Substituting Eq. (A5) into RSF framework yields

$$f_2 - f_{\text{ss}} = a\ln\left(\frac{V_2}{V_{\text{ss}}}\right) - b\log\left(\frac{\sigma_0 + \Delta\sigma_{\text{step}}}{\sigma_0}\right)^{-\frac{\alpha}{b}} \tag{A6}$$

Substituting Eq. (A6) into the Eq. (A4) yields

$$V_2 = V_{\text{ss}}\exp\left(\frac{\Delta\tau_{\text{step}} - f_{\text{ss}}\,\Delta\sigma_{\text{step}} + \alpha(\sigma_0 + \Delta\sigma_{\text{step}})\,\log\left(\frac{\sigma_0 + \Delta\sigma_{\text{step}}}{\sigma_0}\right)}{a(\sigma_0 + \Delta\sigma_{\text{step}})}\right) \tag{A7}$$

Under the assumption of small perturbations $|\Delta\sigma_{\rm step}| \ll \sigma_0$, Eq. (A7) reduces to

$$V_2 \approx V_{\rm ss} \exp\left(\frac{\Delta\tau_{\rm step} - (f_{\rm ss} - \alpha)\,\Delta\sigma_{\rm step}}{a\sigma_0}\right) \tag{A8}$$

In the main text, we neglect the normal-stress dependence of the state variable by setting $\alpha = 0$, which simplifies the expression without affecting the key scaling of the instantaneous velocity response. Also, $\Delta\tau_{\rm step} - f_{\rm ss}\,\Delta\sigma_{\rm step} > 0$ means positive Coulomb stress transfer, which will lead to increase in slip rate, whereas $\Delta\tau_{\rm step} - f_{\rm ss}\,\Delta\sigma_{\rm step} < 0$ is negative Coulomb stress transfer leading to decrease in slip rate of the fault.

The nondimensional tidal perturbation amplitude $P_\sigma = |\Delta\tau - f_*^{ss}\Delta\sigma|/a\sigma_0$ characterizes this instantaneous response of the fault due to tidal loading. However, due to the persistent nature of the tidal loading, the sign of the Coulomb stress $\Delta\tau - f_*^{ss}\Delta\sigma$ for the tidal loading doesn't affect the long-term dynamics of the model and hence the absolute sign of it is taken while defining this nondimensional parameter.

Appendix B Nondimensional equations for the Spring-block model

Balance equations and the friction law for the quasi-dynamics of a spring-block system :

$$\tau_f = \sigma f = k(V_{\rm ss}\,t - \delta) - \eta V + \tau_{\rm p}(t) \tag{B1}$$

$$\sigma = \sigma_0 + \sigma_{\rm p}(t) \tag{B2}$$

$$f = f_0 + a\log\left(\frac{V}{V_0}\right) + b\log\left(\frac{V_0\theta}{d_c}\right), \tag{B3}$$

where tide-induced normal stress perturbations $\sigma_{\rm p}(t)$ and shear stress perturbations $\tau_{\rm p}(t)$ are given by:

$$\sigma_{\rm p}(t) = \Delta\sigma\sin\left(2\pi\frac{t}{T}\right) \quad ; \quad \tau_{\rm p}(t) = \Delta\tau\sin\left(2\pi\frac{t}{T}\right) \tag{B4}$$

By taking the time derivative of the shear stress balance equation B1, we obtain the governing equation for the rate of change of shear stress,

$$\begin{aligned}
\dot\sigma f + \dot f\sigma &= k(V_{\rm ss} - V) - \eta\dot V + \dot\tau_{\rm p} \\
\dot\sigma f + \sigma\frac{\partial f}{\partial V}\dot V + \sigma\frac{\partial f}{\partial\theta}\dot\theta &= k(V_{\rm ss} - V) - \eta\dot V + \dot\tau_{\rm p} \\
f\Delta\sigma\frac{2\pi}{T}\cos\left(2\pi\frac{t}{T}\right) + \sigma\frac{a\dot V}{V} + \sigma\frac{b}{\theta}\dot\theta &= k(V_{\rm ss} - V) - \eta\dot V + \Delta\tau\frac{2\pi}{T}\cos\left(2\pi\frac{t}{T}\right)
\end{aligned} \tag{B5}$$

We introduce $\theta_* = t_* = d_c/V_{\rm ss}$ as the state variable timescale, $V_* = V_{\rm ss}$ as the velocity scale, $f_*^{ss} = f_0 + (a - b)\log(V_{\rm ss}/V_0)$ as the friction coefficient scale. Let tildes denote nondimensional quantities. Thus, V, t and θ in Eq. (B5) are replaced by their nondimensional forms: $V = V_*\widetilde V = V_{\rm ss}\widetilde V$, $t = t_*\widetilde t$, and $\theta = t_*\widetilde\theta$

$$\begin{aligned}
&\frac{2\pi\Delta\sigma}{T}\cos\left(2\pi\frac{t_*\widetilde t}{T}\right)\left[f_0 + a\log\left(\frac{V_{\rm ss}\widetilde V}{V_0}\right) + b\log\left(\frac{V_0\widetilde\theta t_*}{d_c}\right)\right] + \frac{a\sigma\dot{\widetilde V}}{t_*\widetilde V} + \frac{b\sigma\dot{\widetilde\theta}}{\widetilde\theta t_*} \\
&= kV_{\rm ss}(1 - \widetilde V) - \frac{\eta V_{\rm ss}}{t_*}\dot{\widetilde V} + \Delta\tau\frac{2\pi}{T}\cos\left(2\pi\frac{t_*\widetilde t}{T}\right)
\end{aligned} \tag{B6}$$

Multiplying each side of the equation by $t_*/a\sigma_0$, substituting $f_0 + (a - b)\log(V_{\rm ss}/V_0) = f_*^{ss}$, bringing in $k_c =$

$(b-a)\sigma_0/d_c$ and $V_{\rm dyn} = a\sigma_0/\eta$ into the above equation, we get:

$$\frac{\Delta\sigma}{\sigma_0}\frac{2\pi t_*}{T}\cos\left(2\pi\frac{t_*\widetilde{t}}{T}\right)\log\widetilde{V} + \frac{b\Delta\sigma}{a\sigma_0}\frac{2\pi t_*}{T}\cos\left(2\pi\frac{t_*\widetilde{t}}{T}\right)\log\widetilde{\theta} + \frac{\sigma\dot{\widetilde{V}}}{\sigma_0\widetilde{V}} + \frac{b\sigma\dot{\widetilde{\theta}}}{a\sigma_0\widetilde{\theta}}$$
$$= \frac{k}{k_c}\left(\frac{b-a}{a}\right)(1-\widetilde{V}) - \frac{V_{\rm ss}}{V_{\rm dyn}}\dot{\widetilde{V}} + \left(\frac{\Delta\tau - \Delta\sigma f_*^{ss}}{a\sigma_0}\right)\frac{2\pi t_*}{T}\cos\left(2\pi\frac{t_*\widetilde{t}}{T}\right) \tag{B7}$$

We can now clearly identify six nondimensional parameters: $P_T = T/t_*$ (normalized period), $P_\sigma = |\Delta\tau - f_*^{ss}\Delta\sigma|/(a\sigma_0)$ (normalized stress perturbation amplitude), $\epsilon = \Delta\sigma/\sigma_0$ (normalized normal stress perturbation), $\kappa = k/k_c$ (normalized stiffness), $R_{ab} = a/b$ (RSF parameter), and $\mathcal{N} = V_{\rm dyn}/V_{\rm ss}$ (normalized radiation damping). Rewriting the above equation in terms of these parameters, we obtain following nondimensional equation:

$$\frac{2\pi}{\boldsymbol{P_T}}\cos\left(\frac{2\pi\widetilde{t}}{\boldsymbol{P_T}}\right)\left(\boldsymbol{\epsilon}\log\widetilde{V} + \frac{\boldsymbol{\epsilon}}{\boldsymbol{R_{ab}}}\log\widetilde{\theta} - \boldsymbol{P_\sigma}\right) + \frac{\dot{\widetilde{V}}}{\widetilde{V}}\left[1 + \boldsymbol{\epsilon}\sin\left(\frac{2\pi\widetilde{t}}{\boldsymbol{P_T}}\right) + \frac{\widetilde{V}}{\boldsymbol{\mathcal{N}}}\right]$$
$$+ \frac{\dot{\widetilde{\theta}}}{\boldsymbol{R_{ab}}\widetilde{\theta}}\left[1 + \boldsymbol{\epsilon}\sin\left(\frac{2\pi\widetilde{t}}{\boldsymbol{P_T}}\right)\right] = \boldsymbol{\kappa}\left(\frac{1-\boldsymbol{R_{ab}}}{\boldsymbol{R_{ab}}}\right)(1-\widetilde{V}), \tag{B8}$$

with six nondimensional parameters $R_{ab}, \kappa, \mathcal{N}, \epsilon, P_T$, and P_σ.

B.1 Aging law

The evolution of the nondimensional state variable as governed by the aging law,

$$\dot{\widetilde{\theta}} = 1 - \widetilde{V}\widetilde{\theta} \tag{B9}$$

Now using Eq. (B8), substituting the above definition of evolution aging law, we get:

$$\frac{2\pi}{\boldsymbol{P_T}}\cos\left(\frac{2\pi\widetilde{t}}{\boldsymbol{P_T}}\right)\left(\boldsymbol{\epsilon}\log\widetilde{V} + \frac{\boldsymbol{\epsilon}}{\boldsymbol{R_{ab}}}\log\widetilde{\theta} - \boldsymbol{P_\sigma}\right) + \frac{\dot{\widetilde{V}}}{\widetilde{V}}\left[1 + \boldsymbol{\epsilon}\sin\left(\frac{2\pi\widetilde{t}}{\boldsymbol{P_T}}\right) + \frac{\widetilde{V}}{\boldsymbol{\mathcal{N}}}\right]$$
$$+ \frac{1}{\boldsymbol{R_{ab}}\widetilde{\theta}}\left(1 - \widetilde{V}\widetilde{\theta}\right)\left[1 + \boldsymbol{\epsilon}\sin\left(\frac{2\pi\widetilde{t}}{\boldsymbol{P_T}}\right)\right] = \boldsymbol{\kappa}\left(\frac{1-\boldsymbol{R_{ab}}}{\boldsymbol{R_{ab}}}\right)(1-\widetilde{V}) \tag{B10}$$

When we have only shear stress perturbation and $\epsilon \to 0$,

$$\dot{\widetilde{V}} = \frac{\widetilde{V}}{1 + \widetilde{V}/\boldsymbol{\mathcal{N}}}\left[\boldsymbol{\kappa}\left(\frac{1-\boldsymbol{R_{ab}}}{\boldsymbol{R_{ab}}}\right)(1-\widetilde{V}) - \frac{1}{\boldsymbol{R_{ab}}\widetilde{\theta}}\left(1 - \widetilde{V}\widetilde{\theta}\right) + \boldsymbol{P_\sigma}\frac{2\pi}{\boldsymbol{P_T}}\cos\left(\frac{2\pi\widetilde{t}}{\boldsymbol{P_T}}\right)\right], \tag{B11}$$

When there is no stress perturbation, i.e., $\epsilon = 0$ & $P_\sigma = 0$, the above equation reduces to:

$$\dot{\widetilde{V}} = \frac{\widetilde{V}}{1 + \widetilde{V}/\boldsymbol{\mathcal{N}}}\left[\boldsymbol{\kappa}\left(\frac{1-\boldsymbol{R_{ab}}}{\boldsymbol{R_{ab}}}\right)(1-\widetilde{V}) - \frac{1}{\boldsymbol{R_{ab}}\widetilde{\theta}}\left(1 - \widetilde{V}\widetilde{\theta}\right)\right], \tag{B12}$$

with three nondimensional numbers R_{ab}, κ, and N.

B.2 Slip law

The evolution of the nondimensional state variable as governed by the slip law,

$$\dot{\widetilde{\theta}} = -\widetilde{V}\widetilde{\theta}\log(\widetilde{V}\widetilde{\theta}) \tag{B13}$$

Now using Eq. (B8), substituting above definition of evolution slip law, we get

$$\frac{2\pi}{\boldsymbol{P_T}}\cos\left(\frac{2\pi\widetilde{t}}{\boldsymbol{P_T}}\right)\left(\boldsymbol{\epsilon}\log\widetilde{V} + \frac{\boldsymbol{\epsilon}}{\boldsymbol{R_{ab}}}\log\widetilde{\theta} - \boldsymbol{P_\sigma}\right) + \frac{\dot{\widetilde{V}}}{\widetilde{V}}\left[1+\boldsymbol{\epsilon}\sin\left(\frac{2\pi\widetilde{t}}{\boldsymbol{P_T}}\right) + \frac{\widetilde{V}}{\boldsymbol{\mathcal{N}}}\right] - \frac{1}{\boldsymbol{R_{ab}}}\widetilde{V}\log(\widetilde{V}\widetilde{\theta})\left[1+\boldsymbol{\epsilon}\sin\left(\frac{2\pi\widetilde{t}}{\boldsymbol{P_T}}\right)\right] = \boldsymbol{\kappa}\left(\frac{1-\boldsymbol{R_{ab}}}{\boldsymbol{R_{ab}}}\right)(1-\widetilde{V}) \tag{B14}$$

Note that only one term is modified, but it has no impact on the nondimensional parameters.

B.3 Linker-Dieterich evolution law

When we consider the Linker and Dieterich evolution law *(Linker & Dieterich 1992):*

$$\dot{\theta_L} = 1 - \frac{V\theta}{d_c} - \frac{\alpha}{b}\theta\frac{\dot{\sigma}}{\sigma} \tag{B15}$$

The evolution of the nondimensional state variable as follows:

$$\dot{\widetilde{\theta}} = 1 - \widetilde{V}\,\widetilde{\theta} - \boldsymbol{\mathcal{L}}\,\widetilde{\theta}\,\frac{2\pi}{\boldsymbol{P_T}\left[1+\boldsymbol{\epsilon}\sin\left(\frac{2\pi\widetilde{t}}{\boldsymbol{P_T}}\right)\right]}\cos\left(\frac{2\pi\widetilde{t}}{\boldsymbol{P_T}}\right), \tag{B16}$$

where $\boldsymbol{\mathcal{L}} = \alpha\epsilon/b$. Now using Eq. (B8), substituting Equation (B15), we get:

$$\frac{2\pi}{\boldsymbol{P_T}}\cos\left(\frac{2\pi\widetilde{t}}{\boldsymbol{P_T}}\right)\left(\boldsymbol{\epsilon}\log\widetilde{V} + \frac{\boldsymbol{\epsilon}}{\boldsymbol{R_{ab}}}\log\widetilde{\theta} - \boldsymbol{P_\sigma}\right) + \frac{\dot{\widetilde{V}}}{\widetilde{V}}\left[1+\boldsymbol{\epsilon}\sin\left(\frac{2\pi\widetilde{t}}{\boldsymbol{P_T}}\right) + \frac{\widetilde{V}}{\boldsymbol{\mathcal{N}}}\right] + \frac{1}{\boldsymbol{R_{ab}}\widetilde{\theta}}\left[1-\widetilde{V}\,\widetilde{\theta} - \frac{2\pi\alpha\boldsymbol{\epsilon}\widetilde{\theta}}{b\boldsymbol{P_T}\left[1+\boldsymbol{\epsilon}\sin\left(\frac{2\pi\widetilde{t}}{\boldsymbol{P_T}}\right)\right]}\cos\left(\frac{2\pi\widetilde{t}}{\boldsymbol{P_T}}\right)\right]\left[1+\boldsymbol{\epsilon}\sin\left(\frac{2\pi\widetilde{t}}{\boldsymbol{P_T}}\right)\right] \tag{B17}$$

$$= \boldsymbol{\kappa}\left(\frac{1-\boldsymbol{R_{ab}}}{\boldsymbol{R_{ab}}}\right)(1-\widetilde{V}), \tag{B18}$$

where $P_\sigma = [\Delta\tau - (f_*^{ss} - \alpha)\,\Delta\sigma]/a\sigma_0$ is modified nondimensional perturbation amplitude in presence of Linker *(Linker & Dieterich 1992)* effects, which controls the instantaneous response of Coulumb stress transfer to the fault due to the harmonic perturbation.

Rearranging the above equation, we obtain:

$$\frac{2\pi}{\boldsymbol{P_T}}\cos\left(\frac{2\pi\widetilde{t}}{\boldsymbol{P_T}}\right)\left(\boldsymbol{\epsilon}\log\widetilde{V} + \frac{\boldsymbol{\epsilon}}{\boldsymbol{R_{ab}}}\log\widetilde{\theta} - \boldsymbol{P_\sigma}\right) + \frac{\dot{\widetilde{V}}}{\widetilde{V}}\left[1+\boldsymbol{\epsilon}\sin\left(\frac{2\pi\widetilde{t}}{\boldsymbol{P_T}}\right) + \frac{\widetilde{V}}{\boldsymbol{\mathcal{N}}}\right] + \frac{1}{\boldsymbol{R_{ab}}\widetilde{\theta}}\left(1-\widetilde{V}\,\widetilde{\theta}\right)\left[1+\boldsymbol{\epsilon}\sin\left(\frac{2\pi\widetilde{t}}{\boldsymbol{P_T}}\right)\right] = \boldsymbol{\kappa}\left(\frac{1-\boldsymbol{R_{ab}}}{\boldsymbol{R_{ab}}}\right)(1-\widetilde{V}) \tag{B19}$$

As pointed out by *Rice et al. (2001),* and as can be observed in Eq. (A8), $(f_*^{ss} - \alpha)$ acts as an effective friction coefficient

during an instantaneous normal stress change, which comes automatically from above nondimensionalization. Note that the nondimensionalized equilibrium equations remains the similar has 6 nondimensional numbers, however evolution law gives us additional nondimensional number $\mathcal{L} = \alpha\epsilon/b$ which controls the evolution of state variable in presence of normal stress variation.

B.4 Consideration of poroelastic effects in undrained limit

In this undrained limit, the effective normal stress, σ' can be written as

$$\sigma' = \sigma - p = \sigma_0 + \sigma_{\rm p}(t) - (p_0 + \Delta p(t)) = \sigma_0 - p_0 + (1-B)\sigma_{\rm p}(t) = \sigma_0' + (1-B)\sigma_{\rm p}(t), \tag{B20}$$

where σ denotes the total normal stress, decomposed into a background component σ_0 and a time-dependent perturbation $\sigma_{\rm p}(t)$, and p is the pore fluid pressure, consisting of an initial pore pressure p_0 and a perturbation $\Delta p(t)$. The quantity $\sigma_0' = \sigma_0 - p_0$ represents the initial effective normal stress. Under undrained conditions, the pore pressure change induced by the normal stress perturbation satisfies $\Delta p(t) = B\sigma_{\rm p}(t)$, where B is the Skempton's pore pressure coefficient, defined as the ratio of induced pore pressure change to the applied confining stress change *(Segall 2010, Eq. 10.1).*

Now using Eq. (1) of the main text, substituting above definition of effective normal stress and and nondimensionalizing, we get

$$\begin{aligned}\frac{2\pi}{\boldsymbol{P_T}}\cos\left(\frac{2\pi\widetilde{t}}{\boldsymbol{P_T}}\right)\left(\boldsymbol{\epsilon}\log\widetilde{V} + \frac{\boldsymbol{\epsilon}}{\boldsymbol{R_{ab}}}\log\widetilde{\theta} - \boldsymbol{P_\sigma}\right) + \frac{\dot{\widetilde{V}}}{\widetilde{V}}\left[1 + \boldsymbol{\epsilon}\sin\left(\frac{2\pi\widetilde{t}}{\boldsymbol{P_T}}\right) + \frac{\widetilde{V}}{\boldsymbol{\mathcal{N}}}\right] \\ + \frac{1}{\boldsymbol{R_{ab}}\widetilde{\theta}}\left(1 - \widetilde{V}\widetilde{\theta}\right)\left[1 + \boldsymbol{\epsilon}\sin\left(\frac{2\pi\widetilde{t}}{\boldsymbol{P_T}}\right)\right] = \boldsymbol{\kappa}\left(\frac{1-\boldsymbol{R_{ab}}}{\boldsymbol{R_{ab}}}\right)(1-\widetilde{V})\end{aligned} \tag{B21}$$

where $P_\sigma = |\Delta\tau - f_*^{ss}(1-B)\,\Delta\sigma|/a\sigma_0'$, and $\epsilon = (1-B)\,\Delta\sigma/\sigma_0'$

which gives exactly same nondimensional equation as shown in main text. Therefore, entire analysis of main text holds for this case with new definition of nondimensional parameters P_σ and ϵ.

Appendix C Radiation efficiency of a quasi-dynamic spring-block system

While the governing quasi-dynamic equation for the spring-block system Eq. (1) holds at every instant of the time, our primary interest lies in the energy changes accumulated over a finite time window $[t_1, t_2]$, which is identified as a single event based on a velocity threshold criterion. The threshold is chosen such that $V(t_1), V(t_2) \ll V_{\rm dyn} = a\sigma_0/\eta$ so that we attain quasi-static equilibrium at end of time windows of an event. To analyze the energy budget of such an event, we subtract the quasi-dynamic governing equation evaluated at time t_2 from the Eq. (1). This yields an incremental force balance relative to the window endpoint,

$$k\left[(V_{\rm ss}t - \delta) - (V_{\rm ss}t_2 - \delta_2)\right] = (\tau_f - \tau_{f2}) + \eta(V - V_2) - (\tau_{\rm p} - \tau_{p2}), \tag{C1}$$

where $\delta_2 = \delta(t_2), \tau_{p2} = \tau_p(t_2), \tau_{f2} = \tau_f(t_2)$ and $V_2 = V(t_2)$.

The term on the left side in Eq. (C1) can be rewritten as

$$k\left[(V_{\rm ss}t - \delta) - (V_{\rm ss}t_2 - \delta_2)\right] = k(\delta_2 - \delta) + kV_{\rm ss}(t - t_2). \tag{C2}$$

Multiplying Eq. (C1) by the slip rate $V(t)$ gives the incremental power balance,

$$k(\delta_2 - \delta)V + kV_{\rm ss}(t - t_2)V = (\tau_f - \tau_{f2})V + \eta(V - V_2)V - (\tau_{\rm p} - \tau_{p2})V. \tag{C3}$$

Integrating Eq. (C3) over the event duration $[t_1, t_2]$ yields the incremental energy balance. The first spring-related term can be evaluated as

$$\int_{t_1}^{t_2} k(\delta_2 - \delta)\, V\, dt = \frac{1}{2} k(\delta_2 - \delta_1)^2, \tag{C4}$$

where $\delta_1 = \delta(t_1)$.

The second spring-related term involves the background loading and is evaluated using integration by parts,

$$\int_{t_1}^{t_2} kV_{\rm ss}(t - t_2)\, V\, dt = -\, kV_{\rm ss} \int_{t_1}^{t_2} (\delta - \delta_1)\, dt. \tag{C5}$$

Similarly, collecting other terms and using integration by parts, the incremental energy balance over the event window can be written as

$$-\int_{t_1}^{t_2} (\dot{\tau_{\rm p}} + kV_{\rm ss})(\delta - \delta_1)\, dt + \frac{1}{2}\, k\, (\delta_2 - \delta_1)^2 = \int_{t_1}^{t_2} (\tau_f - \tau_{f2})V\, dt + \int_{t_1}^{t_2} \eta(V - V_2)V\, dt. \tag{C6}$$

Equation (C6) represents the energy budget of a velocity-threshold-defined event, expressed in terms of energy increments relative to the window endpoint t_2. This formulation follows directly from quasi-dynamic governing equation and no assumption are made to obtain the above equation. Above equation can be compared to *Kostrov (1974, Eq. 2.24).* The main feature of this equation is that all the terms can be calculated using incremental quantities.

Assuming A [m^2] is the rupture area of the event, the last term in Eq. (C6) corresponds to the radiated energy [Nm] for quasi-dynamic approximation, $E_R = A \int_{t_1}^{t_2} \eta\, (V - V_2)V\, dt \approx A \int_{t_1}^{t_2} \eta\, V^2\, dt$ *(Senatorski 2014, Eq. 7),* if we assume at t_2 the fault satisfy static equilibrium or $V_2 \ll V(t)\ \forall\, t \in (t_1, t_2)$. *Kostrov (1974, Eq. 2.1)* defined the radiated energy as additional work done by a seismic source to its surrounding when the source is active. This energy is the one that is felt in terms of seismic waves on Earth's surface and is present irrespective of speed of the event. The continuum form of the radiated energy and its derivation for quasi-dynamic simulations has been presented in *Kheirdast et al. (2025).* The radiated energy in principle can be calculated from spectra for earthquakes using data from *Abercrombie & Rice (2005).*

The first term on the right side is an observable energy dissipated due to the frictional work [Nm], $D_o = A \int_{t_1}^{t_2} (\tau_f - \tau_{f2})V\, dt = -A \int_{t_1}^{t_2} \dot{\tau_f} (\delta - \delta_1)\, dt$. It is not possible to calculate this quantity directly from observations unless we perform numerical modeling. The second term on the left side is an observable elastic strain energy [Nm], released during the event, $\Delta W_o = A \frac{1}{2}\, k\, (\delta_2 - \delta_1)^2$, which depends on the static stress drop, $k(\delta_2 - \delta_1)$, and the slip during the event $(\delta_2 - \delta_1)$. Note that total strain energy release [Nm] due to an event is $\Delta W_T = A \frac{1}{2} (\tau_{f1} + \tau_{f2})(\delta_2 - \delta_1)$, however it cannot be directly calculated by observations.

Kostrov (1974) originally derived the energy budget equation for ordinary earthquakes with typical duration a few seconds/minutes, and the work done by the external perturbations and tectonic loading [Nm], $\Delta W_{\rm ext} = A \int_{t_1}^{t_2} (\dot{\tau_{\rm p}} + kV_{\rm ss})(\delta - \delta_1)\, dt$, during the event is assumed zero in his derivation. For SSEs, which can have duration of days/months, the external work done can be non-negligible. However, it will be difficult to constrain the exact details of loading in natural observations. Therefore, we write above energy balance as

$$\begin{aligned} \Delta W_o &= D_o + E_R + \Delta W_{\rm ext}, \\ &\approx D_o + E_R. \end{aligned} \tag{C7}$$

D_o is sometimes incorrectly attributed as the "fracture energy" of an event [N/m], $G' := D_o/A \approx (\Delta W_o - E_R)/A$, which is only true if we assume a crack model in an infinite fault with slip weakening friction and most of the frictional dissipation per unit area is happening near the tip of the rupture *(Abercrombie & Rice 2005).* However *Kheirdast et al. (2025),* with their seismic cycle simulation of the fault zone, show that in the presence of off-faults, D_o can contain the contribution due to the interaction of the damage zone with the main fault. Also, rupture arrest mechanisms, incorporating additional physics like thermal pressurization, can significantly contribute to the net magnitude of observable D_o of an event *(Gabriel et al. 2024).*

Venkataraman (2002, Ch. 3.2) and *Kanamori & Heaton (2000)* recommend a working definition of radiation efficiency in terms of observable quantities,

$$\eta_R = \frac{E_R}{\Delta W_o} \approx \frac{E_R}{D_o + E_R}, \tag{C8}$$

which is calculated in our numerical simulations for all the events and average η_R of all events for particular parameters (P_T, P_σ) is shown in Figure 6b. In our numerical simulations, all the terms in the Equation (C6) are computed by defining the path dependent integrands of D_o, E_R, and ΔW_{ext} as state variables of the ODE system so that the running energy balance can be computed in postprocessing between any interval t_1 and t_2. We explicitly verify the validity of the incremental energy balance for each events defined by velocity thresholds and examine the external work term ΔW_{ext} and find that its contribution is negligible in our simulations.

Appendix D Numerical Methods

We solved the governing equations using the `DifferentialEquations.jl` package in Julia (v1.11.0, DifferentialEquations.jl v7.15.0). Time integration was performed with an adaptive explicit Runge–Kutta method (`ExplicitRK`), using the Cash-Karp Butcher table (`tableau=constructCashKarp`) *(Cash & Karp 1990).*

The solver was configured with an absolute tolerance of $\texttt{abstol} = 10^{-14}$ and a relative tolerance of $\texttt{reltol} = 10^{-12}$, together with a maximum iteration limit of $\texttt{maxiters} = 10^9$. Error control was applied only to the physically relevant state variables (τ, V, σ), excluding auxiliary integral variables. The integration interval was set to $t \in [0,\ 20000\, t_*]$, where $t_* = d_c/V_{\text{ss}}$.

In a few simulations, we observe that long sequences of slip events are followed by a transition to persistent stable oscillations. Upon verification, these late-time oscillations are attributed to numerical error accumulation, which cannot be eliminated by further increasing the time-step tolerance. Since such cases are rare, we control for them by requiring a minimum number of slip events so that our overall conclusions remain unaffected.

Appendix E Analysis of slip law

Using the same set of nondimensional parameters as in the aging law case, we find that the overall trends remain consistent for slip law. Triggered events occur only for a limited range of normalized loading periods and when the normalized perturbation amplitude is sufficiently large. However, for identical parameter values, the slip law tends to produce events with systematically higher values of η_R, indicating a greater propensity for high-η_R triggering.

Appendix F Effect of intrinsic nondimensional parameters

In addition to the primary control parameters associated with external stress perturbations, we further investigate the influence of several intrinsic, nondimensional system parameters, including the quasi-dynamic radiation damping $\mathcal{N}$, the nondimensional stiffness κ, and the RSF frictional ratio R_{ab}. These analyses aim to assess the robustness of the main results with respect to variations in fault rheology and dynamic resistance.

Three values of the radiation damping parameter, $\mathcal{N} = 10^3$, 10^6, and 10^9 are tested, which may be interpreted as representing background slip velocity ranging from slow slip rates, through typical tectonic plate convergence rates, to an

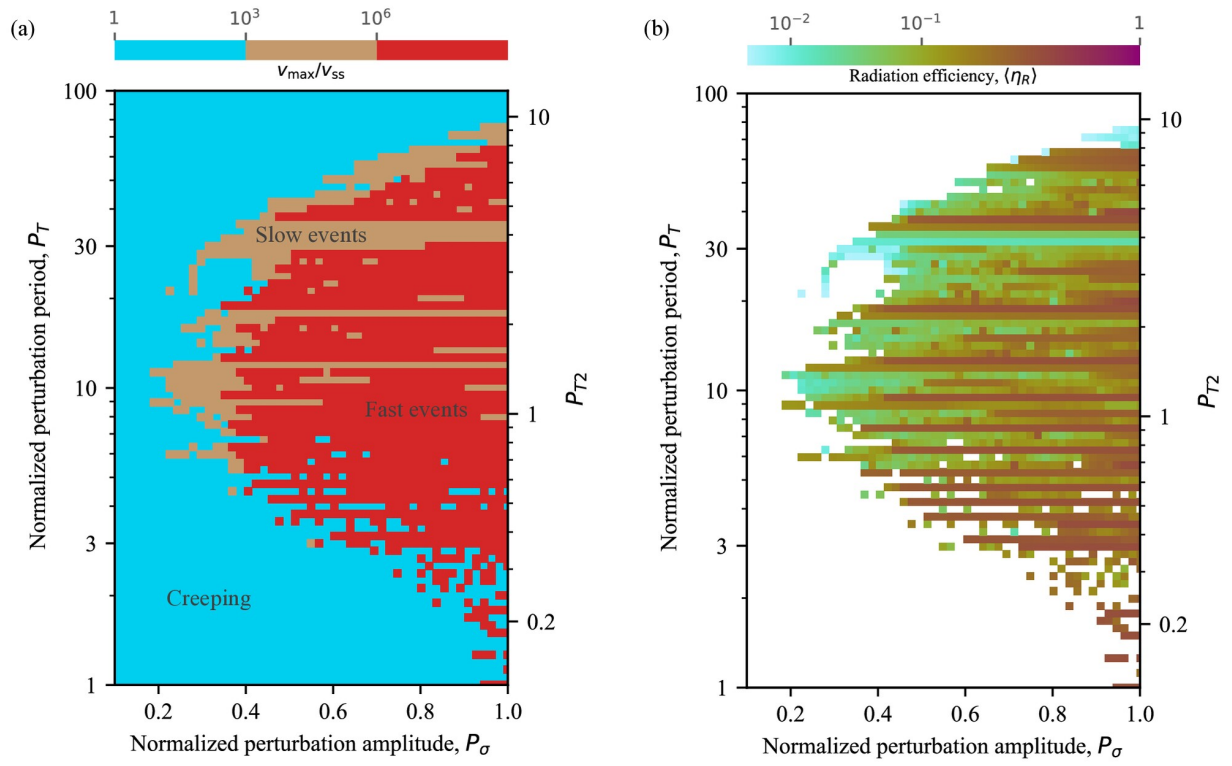

Figure E1: Response phase diagrams of a stable sliding VW fault in the (P_σ, P_T) parameter space under harmonic normal stress perturbations for slip law. (a) Phase diagram colored by the normalized maximum slip velocity $V_{\max}/V_{\rm ss}$. Light blue indicates creeping behavior, brown denotes slow slip events, and red corresponds to fast events.(b) The same parameter space colored by the average radiation efficiency $\langle \eta_R \rangle$, computed only for cases where slip events occur. An event is defined as a slip episode with $V_{\max}/V_{\rm ss} > 10^3$, and $\langle \eta_R \rangle$ represents the mean value averaged over all events in each simulation.

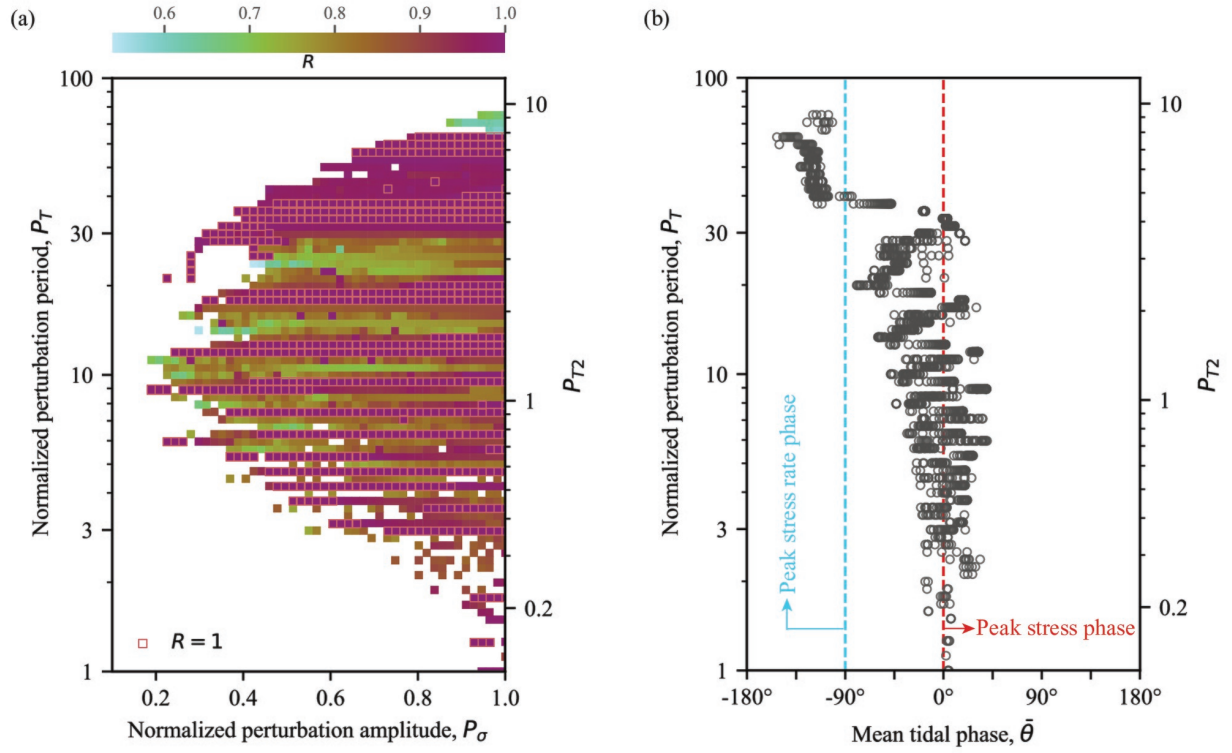

Figure E2: Correlation distribution of triggered events for slip law. (a) Color coded by R, indicating the dispersion of phase values; the closer R is to 1, the higher the concentration around the mean phase. (b) The horizontal axis represents the mean phase, and the vertical axis denotes P_T.

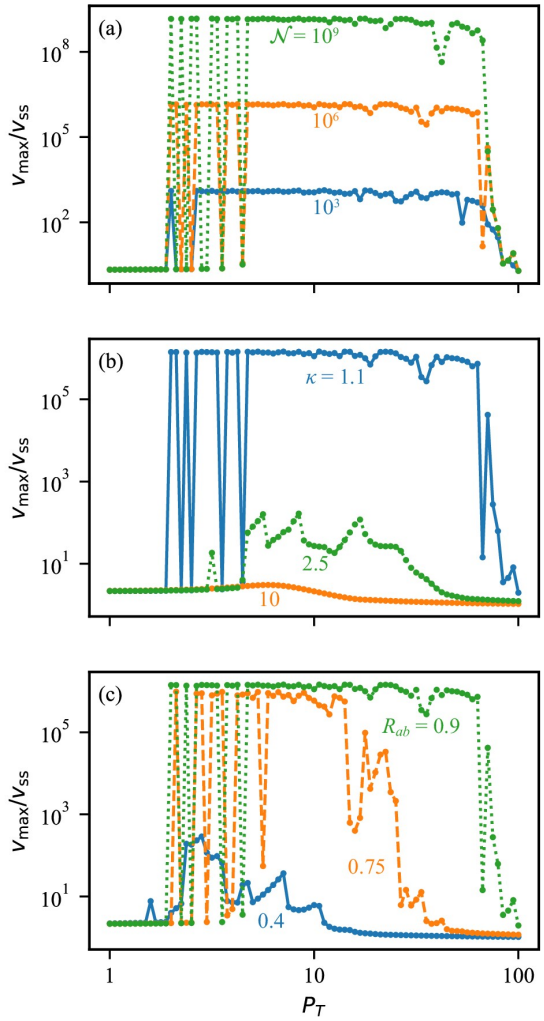

Figure F1: Dependence of the normalized maximum slip velocity $V_{\max}/V_{\rm ss}$ on the normalized perturbation period P_T for (a) different values of $\mathcal{N}$, (b) different values of κ, and (c) different values of R_{ab}. Pronounced fluctuations of $V_{\max}/V_{\rm ss}$, particularly in the range P_T $1-10$, are observed in several cases. These irregular variations are related to the tomb-like structures discussed in the main text, although a detailed analysis of this behavior is beyond the scope of the present figure. Here, the focus is on illustrating how variations in individual parameters affect the overall magnitude and trend of $V_{\max}/V_{\rm ss}$. In each panel, only one parameter is varied, while all other parameters are fixed and consistent with those listed in Table 2.

almost stable sliding regime. As shown in Fig. F1a, $V_{\max}/V_{\rm ss}$ increases systematically with $\mathcal{N}$. Although the scaling is not strictly linear, the overall trend suggests a strong positive dependence of $V_{\max}/V_{\rm ss}$ on $\mathcal{N}$. The effect of system stiffness is examined by varying $\kappa = 1.1$, 2.5, and 10. As illustrated in Fig. F1b, larger values of κ systematically suppress the velocity amplification, indicating a stabilizing influence of increased stiffness. The friction ratio is varied between $R_{ab} = 0.4$ and 0.75. As shown in Fig. F1c, increasing R_{ab} toward unity enhances the slip velocity amplification, indicating that as the system approaches the velocity-neutral transitional regime ($a \approx b$) within the VW domain, the effective frictional resistance to perturbations is reduced, making the fault more susceptible to large slip velocity amplifications.